J. Fluid Mech. (2002), *vol.* 452, *pp.* 371–404.
DOI: 10.1017/S0022112001007017 Printed in the United Kingdom

Constitutive laws in liquid-fluidized beds

By PAUL DURU[1], MAXIME NICOLAS[1], JOHN HINCH[2] AND ÉLISABETH GUAZZELLI[1]

[1]IUSTI, CNRS-UMR 6595, Technopôle Château-Gombert, 13453 Marseille cedex 13, France
[2]DAMTP, University of Cambridge, Silver Street, Cambridge CB3 9EW, UK

(Received 6 May 2001 and in revised form 10 September 2001)

The objective of the present work is to test experimentally the two-phase modelling approach which is widely used in fluidization. A difficulty of this way of modelling fluidized beds is the use of empirical relations in order to close the system of equations describing the fluidized bed as a two-phase continuum, especially concerning the description of the solid phase. We performed an experimental investigation of the primary wavy instability of liquid-fluidized beds. Experiments demonstrate that the wave amplitude saturates up the bed and we were able to measure the precise shape of this voidage wave. We then related this shape to the unknown solid phase viscosity and pressure functions of a simple two-phase model with a Newtonian stress-tensor for the solid phase. We found the scaling laws and the particle concentration dependence for these two quantities. It appears that this simplest model is quite satisfactory to describe the one-dimensional voidage waves in the limited range of parameters that we have studied. In our experimental conditions, the drag on the particles nearly balances their weight corrected for buoyancy, the small imbalance being mostly accounted for by solid phase viscous stress with a much smaller contribution from the solid phase pressure.

1. Introduction

Fluidized beds are widely used in many industrial fields and display a wide range of intriguing phenomena. To fluidize a bed of particles, a fluid is pumped upwards at the bottom of the bed through a porous plate. At low flow rates (below minimum fluidization), the bed is packed. As the flow is increased, the drag force on the particles increases until it is sufficient to balance their weight corrected for buoyancy. The particles then become free to move and the bed is said to be fluidized, and, indeed, the bed can be stirred and poured as if it were a fluid. Uniform and homogeneous fluidized beds are rarely realized in practice. Fluidized beds usually present a variety of complex flow regimes above minimum fluidization. On one hand, gas-fluidized beds are very unstable and rapidly attain a bubbling regime, see Davidson & Harrison (1971). On the other hand, liquid-fluidized beds exhibit a voidage-wave instability. The instability was shown to remain one-dimensional in narrow beds (Anderson & Jackson 1969; Ham *et al.* 1990; Nicolas *et al.* 1996) whereas in wider beds, transverse structures can develop (El-Kaissy & Homsy 1976; Didwania & Homsy 1981). Batchelor (1991) conjectured that bubbles evolve from this secondary instability.

The theoretical description of fluidized systems is an important challenge for physicists and engineers. Noting that the velocity of the particles is on average quite different from the velocity of the fluid, we rapidly conclude that a minimal description of a fluidized bed must be as two coexisting continua, a fluid phase

and a solid phase. Such a two-phase continuum description has been proposed by many before, for a review see Jackson (2001). Attempts have been made to derive two-phase governing equations by averaging separately the equations of motion for the fluid and the particles, for instance Anderson & Jackson (1967). These averaging procedures generate averaged quantities more numerous than the available equations and consequently there is a problem of closure, in particular for the drag force between the phases, for added mass effects, and for the stresses in the two phases. Under practical conditions, where the Reynolds number for the flow past the particle is 10 or more, we know theoretically that the stress at a point must depend on the strain rate at nearby points at previous times, and so a simple expression for the closures cannot exist; exactly the same conceptual problem occurs in turbulence where the eddy-viscosity theoretically cannot exist.

Thus, at best, we are searching for empirical expressions for the closures which are satisfactory within the narrow range of operating conditions of interest. For the drag force between the two phases we use the Richardson–Zaki law, which gives a drag proportional to the difference between the instantaneous values of the velocities of the two phases. The coefficient of proportionality depends on the concentration of the particles. The Richardson–Zaki law has been found over the years to work well. When the particles accelerate relative to the fluid, the fluid exerts a force on the particles proportional to the relative acceleration with a coefficient called the added mass. This added mass has not been studied in concentrated beds. Fortunately, it plays a minor role. We therefore will eventually adopt the value for an isolated sphere equal to half the displaced mass of fluid. The biggest closure problem comes with expressions for the stresses in the fluid and solid phases. We assume like many before that both phases behave as Newtonian viscous fluids. It is clear that the bed as a whole does have a fluid-like behaviour, but it is certainly not clear that both the fluid and solid phases are purely viscous; perhaps the solid phase should have an elastic part. The linearity of the Newtonian stresses in the strain rate is also an assumption whose only justification is that it is the simplest possible alternative.

We note that there are more complicated models introducing a granular temperature and thus a new equation for the 'thermal' energy conservation, for a review see Jackson (2001). It results in a great complexity when trying to derive exact closure relations linking unknown terms to the temperature and to the particle concentration and we think that it is very unlikely that this kind of model could be tested experimentally.

Despite the wide use of models using empirical closure relations, there is a lack of knowledge about the viscosity and the pressure appearing in the Newtonian stress tensor of the solid phase. Several speculative expressions have been proposed since Murray (1965) for the solid viscosity μ_s and the solid pressure p_s, some of them being presented in table 1. Most of these authors chose monotonic functions of the particle volume fraction ϕ which diverge when the particle volume fraction reaches the random close packing volume fraction ϕ_{cp}.

Rough estimates for the unknown solid viscosity and pressure were obtained by studying the voidage-wave instability occurring in narrow liquid-fluidized beds (Anderson & Jackson 1969; El-Kaissy & Homsy 1976). The voidage disturbances were found to grow exponentially up the bed and eventually to saturate at their finite amplitude. By measuring their propagation properties and the general growth and comparing with linear stability theory, these authors were able to estimate parameters appearing in the assumed constitutive equations. However, these measurements did not give any insight on the shape of the functions $\mu_s(\phi)$ and $p_s(\phi)$ as they only provided values for a few particle concentrations ϕ.

Authors	$p_s(\phi)$	$\mu_s(\phi)$
Murray (1965)	0	$\mu_f \dfrac{M\phi}{\phi_{cp}-\phi}$
Fanucci *et al.* (1981)	Not given	$M \exp\left[\dfrac{\phi_{cp}-\phi}{(1-\phi_{cp})(1-\phi)}\right]$
Needham & Merkin (1983)	$P\phi$	Constant
Harris & Crighton (1994)	$P\phi/(\phi_{cp}-\phi)$	Constant
Anderson *et al.* (1995)	$P\phi^3 \exp\left(\dfrac{r\phi}{\phi_{cp}-\phi}\right)$	$\dfrac{M\phi}{1-(\phi/\phi_{cp})^{1/3}}$
Glasser *et al.* (1996)	$\begin{cases} C_1\phi^3 \exp\left(\dfrac{r\phi}{\phi_{cp}-\phi}\right) \\ C_2\phi \\ C_2 \dfrac{\phi}{(\phi_{cp}-\phi)^2} \end{cases}$	$\dfrac{M\phi}{1-(\phi/\phi_{cp})^{1/3}}$

TABLE 1. Various expressions for p_s and μ_s proposed in the literature.

The two-phase model has also been tested as a whole, by simulating the fully nonlinear two-phase equations with different closure relations for the solid viscosity and the solid pressure (Anderson *et al.* 1995; Glasser, Kevredikis & Sundaresan 1996, 1997). Glasser *et al.* (1997) have notably shown that two-dimensional bubble-like solutions were stationary solutions of the two-phase equations in both liquid and gas cases. However, these structures could be reached only in this latter case, either by a two-dimensional destabilization of the uniform bed or by a two-dimensional destabilization of the fully developed one-dimensional plane wave, these mechanisms failing to produce bubbles in the liquid-fluidized case. The two-phase equations, along with these *ad hoc* closure relations seem to succeed in reproducing some important experimental facts. It should be noticed that the added mass term was omitted in their numerical simulations, even in the liquid-fluidized bed case.

The approach we adopt in this paper is different. We study experimentally the voidage-wave instability and show that the voidage disturbance, after its initial growth, reaches a nonlinearly saturated shape which we are able to measure with accuracy. We then relate this saturated shape to the unknown parameters of the two-phase model and are thus able to recover the viscosity and the pressure of the solid phase. Hence, we find the form and the scaling laws for the viscosity and the pressure. Our experiments can thus be viewed as a restricted test of the two-phase model of a fluidized bed.

This paper is organized as follows. First, we present the measurements of the accurate shape of the voidage wave propagating in a narrow liquid-fluidized bed. This is an important result since this wave shape has never been measured experimentally before, but was rather obtained by numerical simulations. Our experimental set-up is presented in § 2. It depends on the fact that such an instability is known to be convective (Nicolas *et al.* 1994, 1996). The influence of the experimental parameters on the nonlinearly saturated wave is presented in § 3. Then, in § 4, we show how to relate the saturated wave-shape to the unknown solid viscosity and solid pressure functions appearing in the two-phase equations. The results concerning the solid

Set	d_s (μm)	ρ_s (g cm^{-3})
A	1220 ± 60	4.08 ± 0.01
B	928 ± 100	4.08 ± 0.01
C	685 ± 30	4.08 ± 0.01
D	1200 ± 90	2.48 ± 0.01
E	771 ± 40	2.55 ± 0.01

TABLE 2. Particle characteristics.

Fluid	*A* (% of glycerol)	μ_f (cP)	ρ_f (g cm^{-3})
a	0	0.9 ± 0.02	0.997 ± 0.002
b	35	3 ± 0.2	1.1 ± 0.03

TABLE 3. Fluid characteristics.

viscosity μ_s are presented in § 5 and those concerning the solid pressure p_s in § 6. Section 7 contains our discussion of the results.

2. Experimental techniques

2.1. *Particles and fluids*

Experiments were performed with different sets of glass beads having different densities ρ_s and diameters d_s. Characteristics of the particles are presented in table 2. Sets *A*, *B* and *C* were supplied by Cataphote (Jackson, MS, USA), set *E* by J.-C. Borgotti of Laboratoire Central des Ponts et Chaussées (Paris, France), and set *D* by Matrasur (Palaiseau, France). The beads were supplied presieved and were further carefully resieved between two close meshes. The bead diameter distribution was obtained from measurements of 300 beads with a charged coupled device camera and a digital imaging system composed of an acquisition board and of the public domain image processing NIH Image†. The distributions were all found to be approximately Gaussian with mean diameter d_s. The standard deviation was taken as the experimental error in the diameter. The particle density ρ_s was determined by measuring the volume variation when a known mass of particles was introduced into a known volume of water in a graduated vessel.

In order to examine the influence of the viscosity of the fluid, we used two fluids: pure water and a mixture of glycerine and water. The temperature of the fluids was maintained at 27 ± 1 °C by using a thermostatically controlled bath as a fluid reservoir in the fluid circulating loop of the fluidized bed (see § 2.2). Characteristics of the two fluids are displayed in table 3.

2.2. *Apparatus*

The fluidized bed apparatus, which is sketched in figure 1, was derived from that of Nicolas *et al.* (1996), itself derived from that of Ham *et al.* (1990). The fluidized bed was a straight and vertical cylindrical glass tube of height 1.8 m mounted on a rigid support structure. Different tubes having different inner diameters *D* were used in the experiments, as indicated in table 4. The bed to particle diameter ratio,

† Public domain NIH Image program, developed at the US National Institute of Health and available from the Internet by anonymous ftp from zippy.nimh.nih.gov.

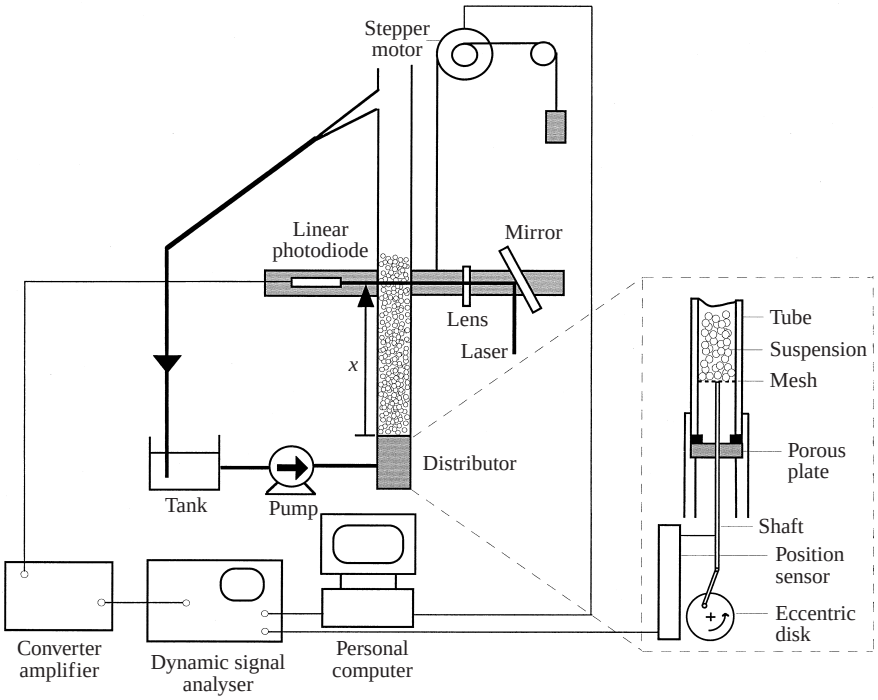

FIGURE 1. Sketch of the fluidized bed apparatus.

Tube	D (cm)
1	3.0 ± 0.02
2	1.5 ± 0.02
3	0.7 ± 0.02

TABLE 4. Tube characteristics.

D/d_s, was chosen to be smaller than 25 in order to ensure that the instability remains one-dimensional and larger than 10 in order to avoid the particle arching effect within the tube (see § 3.1). This ratio falls into the ratio range used in the previous experiments of Ham *et al.* (1990) for which wall effects were considered negligible while maintaining a good resolution of the light attenuation technique (see § 2.3). The different tubes were inspected to ensure that their cross-sections were round and constant along their lengths.

Fluid was circulated through the bed by a piston metering pump (Fluid Metering Inc. model QD, 1425 r.p.m), used to produce flow rates up to $7\,\mathrm{dm}^3\,\mathrm{min}^{-1}$. Soft tubing was placed upstream of the bed in order to isolate the bed from pump vibrations. Soft tubing also connected the overflow at the top of the bed and carried it to the reservoir. It provided an easy way of diverting the entire overflow into a beaker for gravimetric flow measurements.

The suspension was held by a piston composed of a mesh with holes smaller than the size of the beads. This piston could be either kept immobile or moved with a sinusoidal motion at a given frequency by an eccentric disk driven by a d.c. motor (see the blow-up in figure 1). The uniform distribution of the flow was provided by

Frequency	Relative power	Relative amplitude
f_0	1	1
$2f_0$	0.025	0.153
$3f_0$	0.018	0.136
$4f_0$	0.002	0.048

TABLE 5. Power spectrum of the displacement signal of the piston. The frequency f_0 is the forcing frequency.

a fixed porous plate located before the piston. The pores in the porous plate were small enough to ensure a large pressure drop. This piston-type distributor was used to study the response of the fluidized bed to a local harmonic forcing. When the piston moved upwards, it created a local compression of the fluidized particles, and when it moved downwards, it created a local deficit of particles. This local perturbation was then convected by the flow and spatially amplified along the fluidized bed (if the mode was unstable), see Nicolas *et al.* (1996). Since the piston was in fact a thin mesh, it did not induce significant variation of the flow rate.

The amplitude of the displacement of the piston had to be carefully selected. It had to be larger than the amplitude of the 'natural' noise which was always present at the distributor. On the other hand, if the amplitude (or the mean particle concentration) was too large, the motion of the piston created contacts between particles and therefore local close packing just above the piston, in particular for small bed to particle diameter ratio D/d_s. In the latter case, the beads may stay jammed in the tube owing to arching effects, which stops the propagation of the perturbation. Typically, in the present experiments, the amplitude of the piston was chosen to be $\approx 1.5d_s$. The motion of the piston was measured with the use of a linear displacement gauge (Novotechnic model T25) and an electronic circuit provided a reference phase signal used to trigger the concentration measurements (see § 2.4). It should be mentioned that, because of the flexibility of the shaft holding the piston and the small size of the eccentric gear, the motion of the piston was not perfectly sinusoidal but presented few harmonics, as indicated in table 5.

2.3. *Particle volume fraction measurements*

The mean particle volume fraction, ϕ_0, was estimated by measuring the fluidized bed mean height, h_0. In a steady state regime of fluidization, the front between the fluidized particles and the clear fluid at the top of the bed was observed to exhibit fluctuations (due to the wave instability) around a fixed mean height. This mean height of the suspension, h_0, was measured with a viewfinder mounted on a horizontal optical rail which could slide along the bed on two vertical rails. The position of the optical rail and therefore of the view-finder was determined with the use of a ruler attached along the bed with an accuracy of 0.5 mm. The mean volume fraction was then given by $\phi_0 = 4M_s/(\pi D^2 \rho_s h_0)$ where M_s is the weight of the particles. The mean particle volume fraction, ϕ_0, was measured before and after any instability wave measurement. The relative error in ϕ_0 is $\approx 2\%$.

In order to determine the local particle volume fraction, $\phi(x,t)$, at time t and position x from the mean position of the piston-type distributor, measurements of the attenuation of light through the suspension were performed. The basic principle behind this light attenuation technique is that the amount of light attenuation by particles in a suspension is a function of the particle concentration (see for instance

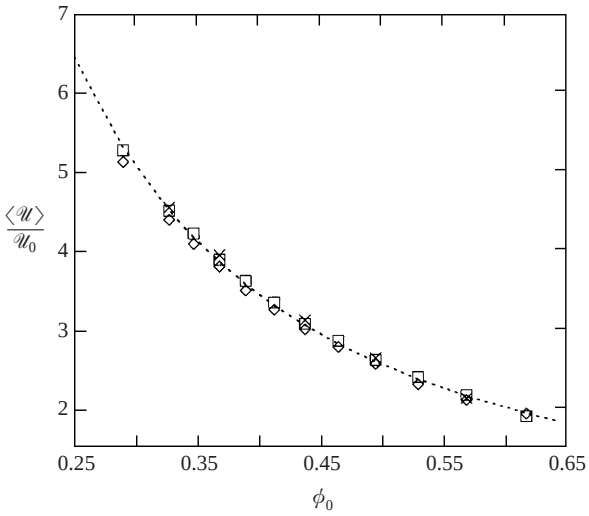

FIGURE 2. Calibration of the averaged signal, $\langle \mathscr{U} \rangle$, with the mean volume fraction, ϕ_0 at $\diamond$, $x = 5$ cm; $\square$, 10 cm; $\times$, 15 cm. The dotted curve corresponds to the best power law correlation, ϕ_0^{ξ} with $\xi = -1.35$ for combination 6.

Combination	Particles	Fluid	Tube	$\xi(\pm 0.1)$
1	*A*	*a*	1	−2.30
2	*A*	*b*	1	−2.15
3	*D*	*a*	1	−3.35
4	*B*	*a*	2	−1.80
5	*B*	*b*	2	−1.60
6	*C*	*a*	2	−1.35
7	*C*	*a*	3	−1.50
8	*E*	*a*	2	−1.60

TABLE 6. Value of ξ for all different combinations of particles, fluid and tube used in the present work.

the use of this technique in the case of fluidized beds by Anderson & Jackson 1969 and El-Kaissy & Homsy 1976, and in the case of sedimenting suspensions by Davis & Birdsell 1988). The light source was a 25 mW He-Ne stabilized laser (Spectra Physics 107B). The laser beam was incident at right angles on the bed glass tube and illuminated the tube with a 4 mm diameter round spot using a diverging lens.

A linear photodiode (Hewlett–Packard model 508-4220 PIN) was used to detect the transmitted light through the suspension. The photodiode was aligned opposite the laser beam along the same bed diameter. The lens and the photodiode were mounted on the optical rail which could slide along the bed. The motion of the rail was driven by a stepping motor which itself was monitored by a personal computer. The smallest available displacement corresponding to one step was 0.3 mm. The intensity signal from the photodiode was processed by a converter/amplifier electronic circuit which converted the micro-ampere current signal from the photodiode to a voltage signal, $\mathscr{U}$, for further processing.

The voltage signal was averaged over 160 s, a time much larger than the wave instability period. The averaged value $\langle \mathscr{U} \rangle$ was measured at a given position x as

a function of the mean particle volume fraction, ϕ_0. The resulting plot which is presented in figure 2 is a monotonically decreasing function which was used to calibrate the light attenuation through the suspension. The best fit was found in each case to be a power law correlation: $\langle \mathscr{U} \rangle = \mathscr{U}_0 \phi_0^{\xi}$ with ξ depending on the beads, the fluid, and also the tube, see table 6.

However, owing to a small misalignment of the glass tube (and probably a small variation of the tube thickness), the light transmission through the tube without particles was not observed to be the same at different location along the tube, i.e. $\mathscr{U}_0$ varied with x. Therefore, $\langle \mathscr{U} \rangle$ was normalized by $\mathscr{U}_0$ at each position x and $\langle \mathscr{U} \rangle / \mathscr{U}_0$ did not vary along the tube, as shown in figure 2. For each position x, the local volume fraction was then given by

$$\phi(x,t) = \frac{\phi_0}{\langle \mathscr{U}(x,t) \rangle^{1/\xi}} \mathscr{U}(x,t)^{1/\xi}, \tag{2.1}$$

where the brackets note a temporal average over several periods.

2.4. *Wave instability measurements*

In order to obtain quantitative measurements of the wave instability, the recording of the signal $\mathscr{U}$ over a few wave periods was synchronized with the piston-type distributor. A digital signal analyser (Hewlett–Packard model 3562A) in a triggering mode was used to record the signal $\mathscr{U}$ at a given position x along the bed. In this triggering mode, time recording started when the forcing phase was zero (i.e. when the piston was in its average position and moving upwards). The signal analyser was controlled by the personal computer through an IEEE board. Each time recording was transferred to the personal computer and converted to concentration values using the calibration, see equation (2.1). The resulting concentration signal was then averaged over typically 30 or 100 recordings depending upon the desired accuracy of the measurements (30 for the study of the wave evolution, see § 3.2, and 100 for the study of the saturated wave, see § 3.3). This synchronized averaging technique provided the waveform of the mode which is correlated with the frequency of the forcing.

2.5. *Wave velocity measurements*

The wave propagation can also be visualized by backlighting the column with a neon light. A CCD camera captures a one-dimensional image of the tube and the digital imaging system is able to construct spatiotemporal plots from successive one-dimensional images. On such plots, see figure 3, clear lines correspond to low concentration regions of the fluidized bed moving upwards and the measurement of their constant slope gives the wave velocity c.

2.6. *Experimental procedure*

Once a weighted amount of particles was introduced into the bed, fluid was circulated through the bed at a flow rate sufficient to expand the bed to the top of the tube. The bed was operated in this expanded state for about 20 min to remove any small trapped air bubbles or impurities.

After the start-up procedure, the expansion behaviour of the bed was measured. The flow rate of the bed was lowered in different steps. At each step, the bed was allowed to come to a steady state with a constant height of the bed. The flow rate was then measured gravimetrically and the bed height measured. The flow rate examined ranged between the initial expanded state and a completely packed bed.

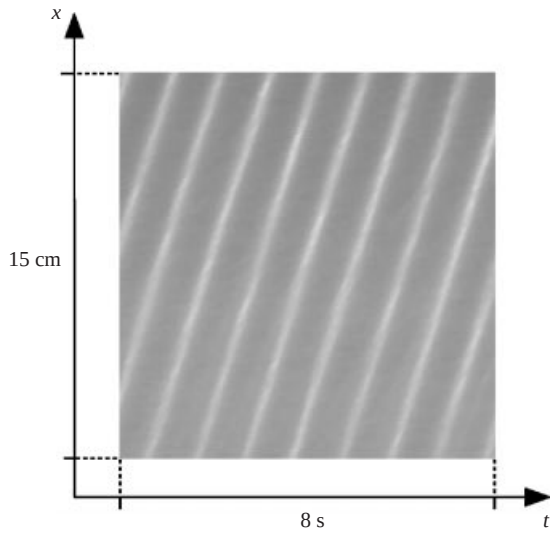

FIGURE 3. Spatiotemporal plot obtained with combination 2 and $\phi_0 = 0.540$. The wave is forced at 1 Hz. Only 15 cm of the bed, shot during 8 s, are shown.

Wave instability measurements were performed at a fixed flow rate (or particle volume fraction) and a given frequency of forcing. The wave mode correlated with the frequency of the forcing was measured along the bed, the use of the personal computer for controlling the signal acquisition and the motion of the optical rail ensuring reproducibility of the measurements.

3. Spatial evolution of the voidage wave instability

3.1. *Fluidized bed expansion*

As previously noted in the fluidized bed literature, see Didwania & Homsy (1981) and Ham *et al.* (1990) for instance, four different regimes were observed during the expansion of the bed. Typical expansion data showing superficial velocities q versus mean particle volume fractions ϕ_0 are presented in figure 4. The expansion curve can be fitted well by the empirical Richardson–Zaki relation $q = v_t(1 - \phi_0)^n$. The exponent n and terminal velocity v_t were measured by using this fit for the mean volume fraction range corresponding to the waves studied in § 3.3. The expansion characteristics are given in table 7 for all the different combinations of particles, fluid, and tube used in the present work.

Below the minimum fluidization velocity q_{mf}, the bed remained packed at the bottom of the tube, with a mean particle volume fraction ϕ_{mf}. This volume fraction corresponded to a random loose packing of the beads. With a gentle tapping of the tube, a random close packing was obtained, with a mean particle concentration ϕ_{cp}. This maximum value was below the classical value of a random close packing of monodisperse spheres (≈ 0.64) because the suspension is constrained by the small bed to particle size ratio.

For a fluid velocity slightly above q_{mf}, the top of the packing started to move, but the bottom of the suspension stayed still. The liquid then crossed the suspension of packed beads through preferential paths. This regime was called 'worming' fluidization, see Ham *et al.* (1990). The value of q_{mf} was taken to be the velocity at which the bed

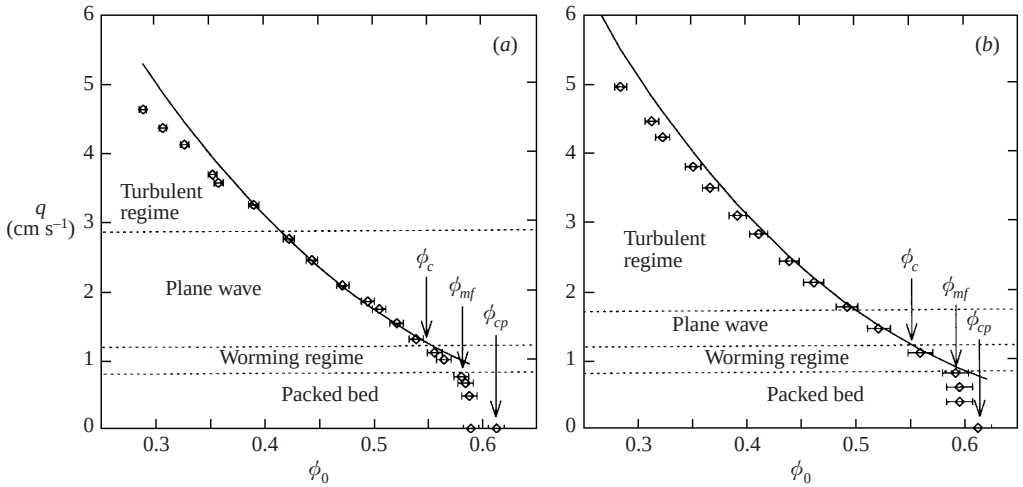

FIGURE 4. Expansion curve of the fluidized bed: (*a*) combination 7, $D/d_s = 10$; (*b*) combination 6, $D/d_s = 22$. The solid line corresponds to the Richardson–Zaki law.

Combination	Particles	Fluid	Tube	D/d_s	v_t (cm s^{-1})	n	ϕ_{cp}	ϕ_{mf}	ϕ_c
1	*A*	*a*	1	25	21.55 ± 0.35	2.43 ± 0.03	0.630	0.608	0.578
2	*A*	*b*	1	25	20.4 ± 0.25	3.18 ± 0.02	0.627	0.610	0.560
3	*D*	*a*	1	25	14.4 ± 0.20	2.58 ± 0.03	0.630	0.588	0.555
4	*B*	*a*	2	16	17.7 ± 0.30	2.84 ± 0.02	0.615	0.590	0.545
5	*B*	*b*	2	16	17.4 ± 0.40	3.65 ± 0.10	0.600	0.565	0.520
6	*C*	*a*	2	25	16.4 ± 0.40	3.25 ± 0.04	0.612	0.580	0.555
7	*C*	*a*	3	10	15.7 ± 0.20	3.18 ± 0.02	0.613	0.589	0.543
8	*E*	*a*	2	19	12.0 ± 0.20	3.30 ± 0.02	0.614	0.575	0.544

TABLE 7. Fluidized bed expansion characteristics. The experimental uncertainty on ϕ_{cp}, ϕ_{mf} and ϕ_c is ± 0.005.

begins to expand and was measured by identifying the break in the expansion curve, see figure 4.

As the flow rate was increased, the whole suspension was fluidized and started to exhibit the primary voidage wave instability where a concentration plane wave propagated upwards along the bed at a flow rate q_c corresponding to a volume fraction ϕ_c. For the type of particles and fluids used in the present experiments, no stable regime of fluidization such as observed by Ham *et al.* (1990) was present.

For an even larger flow rate, the wavy instability no longer existed and the particles exhibited large and random displacements. This regime has been called the turbulent regime.

It should be stressed that instability threshold and range are strongly dependent upon aspect ratio D/d_s. When D/d_s is small (~ 10), as in combination 7 (see figure 4*a*), confinement effects tend to stabilize the plane wave. In this case, the ϕ_0-range for which the waves are observed is much larger than in the cases of larger values of D/d_s (for instance for the case $D/d_s \sim 22$ shown in figure 4*b*). Also, for $D/d_s \sim 10$, if ϕ_0 was too large, the upward motion of the piston created close packing in the bottom of the dense suspension and the beads can become jammed in the tube owing to arching effects, which stops the propagation of the perturbation, as mentioned earlier. The forcing method was no longer efficient and the waves cannot be measured. Therefore,

Combination	ϕ_0	$c\,(\mathrm{cm\,s^{-1}})$	ϕ_{max}	Amplitude	$f_0\,(\mathrm{Hz})$	$Re\ (v_t d_s \rho_f/\mu_f)$
1	0.57	7.30 ± 0.15	0.606	0.104	1.4	287
1	0.558	7.95 ± 0.10	0.603	0.127	1.4	287
1	0.55	8.15 ± 0.10	0.598	0.126	1.4	287
2	0.548	5.60 ± 0.10	0.566	0.052	1.03	82
2	0.540	5.95 ± 0.05	0.563	0.061	1.00	82
2	0.538	5.90 ± 0.10	0.564	0.066	1.06	82
2	0.528	6.05 ± 0.20	0.555	0.062	1.07	82
3	0.545	4.96 ± 0.04	0.570	0.07	1.00	192
3	0.540	5.00 ± 0.05	0.564	0.064	1.05	192
3	0.535	5.25 ± 0.07	0.565	0.074	1.10	192
3	0.531	5.30 ± 0.07	0.561	0.074	1.10	192
4	0.527	5.95 ± 0.05	0.555	0.087	1.6	182
4	0.519	6.00 ± 0.05	0.551	0.094	1.8	182
4	0.512	6.15 ± 0.10	0.546	0.11	1.5	182
5	0.504	4.50 ± 0.04	0.522	0.045	1.3	54
5	0.499	4.60 ± 0.10	0.519	0.054	1.2	54
6	0.549	4.70 ± 0.15	0.575	0.082	1.1	125
6	0.549	4.30 ± 0.10	0.576	0.065	1.55	125
6	0.549	3.90 ± 0.10	0.568	0.035	2.2	125
6	0.534	4.70 ± 0.10	0.564	0.083	1.25	125
6	0.534	4.60 ± 0.10	0.565	0.078	1.62	125
6	0.525	4.90 ± 0.10	0.554	0.084	1.40	125
7	0.488	3.7 ± 0.1	0.522	0.082	2.1	120
7	0.496	3.8 ± 0.2	0.528	0.096	1.54	120
8	0.530	3.47 ± 0.03	0.548	0.077	1	103
8	0.521	3.59 ± 0.03	0.549	0.082	1	103
8	0.521	3.60 ± 0.03	0.548	0.077	1	103
8	0.521	3.64 ± 0.03	0.547	0.080	1.1	103
8	0.512	3.75 ± 0.10	0.545	0.087	1	103
8	0.511	3.80 ± 0.05	0.540	0.080	1	103
8	0.507	3.75 ± 0.05	0.541	0.082	1.25	103

TABLE 8. Saturated wave characteristics. The experimental uncertainty on ϕ_{max} and on the wave amplitude is estimated to be ± 0.003. Within a given combination, the uncertainty on ϕ_0 is ± 0.003, corresponding to the error on the measure of the height of the bed. When comparing two different combinations, we must also take into account the error on the total mass of beads and the density of the beads which leads to a global uncertainty of ± 0.01.

in this case, waves were measured further above the instability threshold ϕ_c (see table 8). When D/d_s was larger (typically between 16 and 25, which is the case for all combinations except combination 7), transverse destabilizations of the plane wave occurred in earlier stages as the flow rate was increased. It was nonetheless possible to study the plane waves but the corresponding ϕ_0-range was quite restricted, see figure 4(*b*). Plane waves were thus observed and measured in regions closer to the instability threshold ϕ_c.

3.2. *Nonlinear evolution of the voidage wave instability*

Since the instability is convective in nature as demonstrated by Nicolas *et al.* (1996), any perturbation created at the bottom of the bed ('natural' noise or controlled

perturbation) propagates and evolves along the bed. The behaviour of the fluidized bed was then analysed by investigating the response of the suspension to a localized and controlled perturbation produced by the forcing distributor (see § 2.2). The spatial evolution of each forced mode was investigated independently. The synchronized average method described in § 2.4 was used to separate the forced mode from the 'natural' noise. This 'natural' noise is indeed always present at the bottom of the bed, also grows along the height of the bed, and participates in the nonlinear behaviour of the wave.

For a given mean volume fraction, three types of behaviour were observed depending upon the forcing frequency f_0. For large frequencies above a cutoff frequency, the wave amplitude decayed along the bed. Figure 5 shows the spatial evolution of such a stable mode. After a short length of propagation, the amplitude of this mode of high frequency vanished. It is important to notice that the decay of the stable mode amplitude is far from being exponential within the range of amplitudes which we could observe. The propagation of a neutral mode is shown on figure 6. Such a mode is propagating along the fluidized suspension without change of amplitude or shape. Finally, figure 7 shows an example of an unstable mode for which the amplitude is observed to grow and the shape to evolve. Once again, no range of exponential growth of the amplitude could be observed. The wave evolution is rapidly dominated by nonlinearities. We will focus on the unstable modes in the following sections of the paper.

The stability diagram for the combination 7 of table 7 summarizes the three types of modes and is given in figure 8 where the neutral curve separates two half-planes in the (ϕ_0, f_0) coordinates. The neutral curve $f_n(\phi_0)$ is a straight line. For large volume fraction, this line crosses the zero-frequency line at a volume fraction which is close to the value ϕ_c corresponding to the onset of the wavy instability (see § 3.1). Stability diagrams were not collected for the other combinations of table 7 because the ϕ_0 ranges were very restricted. The present experiment focused on the nonlinear saturated waves described in the following section.

3.3. *Nonlinear saturation of the unstable modes*

The shape and amplitude of an unstable mode evolve along the bed. Close to the moving piston, the forced perturbation is symmetrical (with respect to the mean volume fraction) in shape, as can be seen on figure 7(*a*). At a short distance above the distributor, the wave loses its symmetry and its amplitude grows, as can be seen in figure 7(*b*,*c*). It then saturates as can be seen in figure 7(*d*,*e*). It is important to mention that the saturated amplitude of the mode is an intrinsic quantity. If the amplitude of the forcing at the bottom of the bed is smaller than the saturated amplitude, the mode amplitude grows to reach the saturated value. If the amplitude of the forcing is larger than the saturated amplitude, the mode amplitude decays to reach also the saturated value.

As can be seen in figure 9, which is typical of many further observations, the saturated wave can be described as a succession of concentration dips and plateaux and present a slight asymmetry. A summary of the characteristics of the saturated waves is presented in table 8 for different combinations of particles, fluids and beds as well as for different mean volume fractions ϕ_0 and forcing frequencies f_0. In order to increase the measurement accuracy, 100 synchronized averages were performed to obtain the shape of the saturated waves. It should be mentioned also that for low forcing frequencies, as the unstable wave grows, a secondary minimum can occur and become important, see figure 10. It was verified that this secondary minimum

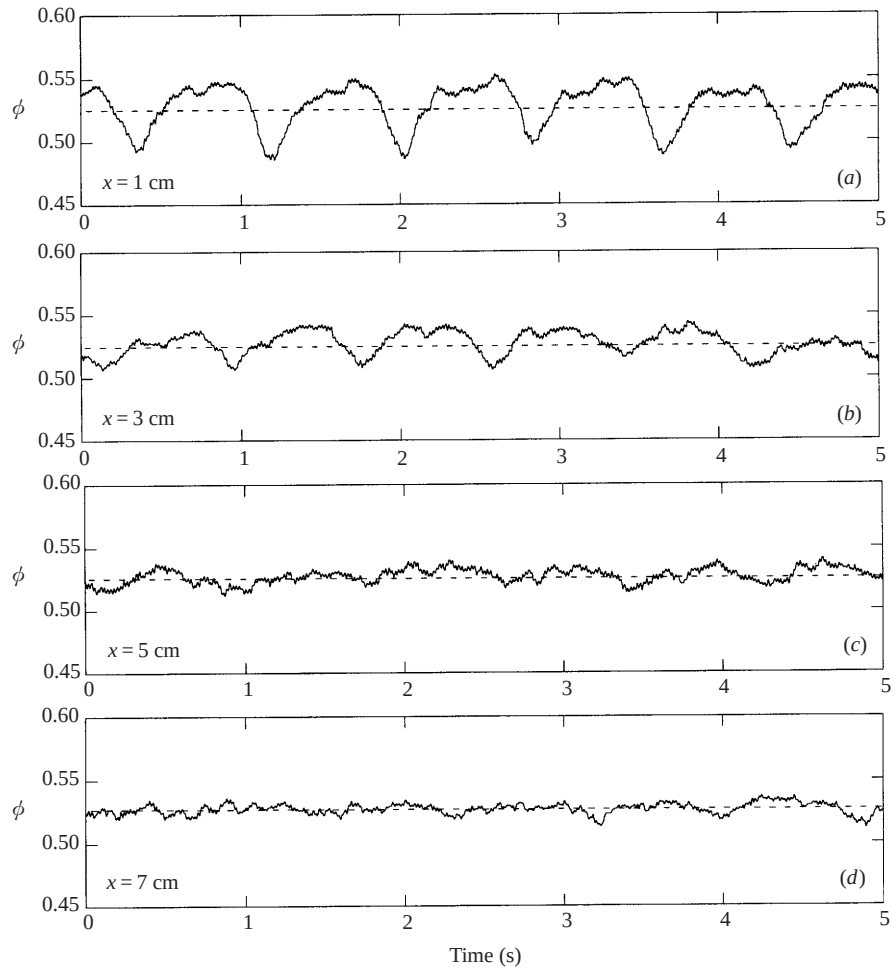

FIGURE 5. Spatial evolution of a stable mode. This stable mode was obtained when using combination 7 of particles, fluid and tube, with $\phi_0 = 0.524 \pm 0.002$ and $f_0 = 1.22$ Hz. The wave shape was measured at different positions x along the bed and obtained by averaging over 30 time sequences.

was due to the growing $2f_0$ mode produced by the imperfect moving piston (see table 5). When $2f_0 > f_n(\phi_0)$, this first harmonic is damped and does not produce any secondary minimum.

The phase velocity was measured by the digital image processing system, as already explained in § 2.5. It does not seem to vary much along the bed, but spatio-temporal diagrams were nonetheless built from images near the top of the fluidized bed, where we knew for sure that the waves were fully saturated.

3.4. *Experimental shape of the waves as a function of experimental parameters*

The main characteristics of the saturated waves are presented in table 8. For a given set of particles, the shape of the saturated wave depends upon the values of experimental parameters, namely the mean particle concentration ϕ_0, the forcing frequency f_0 and the fluid viscosity μ_f. It should be stressed that the value of the mean particle concentration is chosen in a range for which the wavy instability is observed naturally, i.e. without forcing, within the bed. This concentration is thus

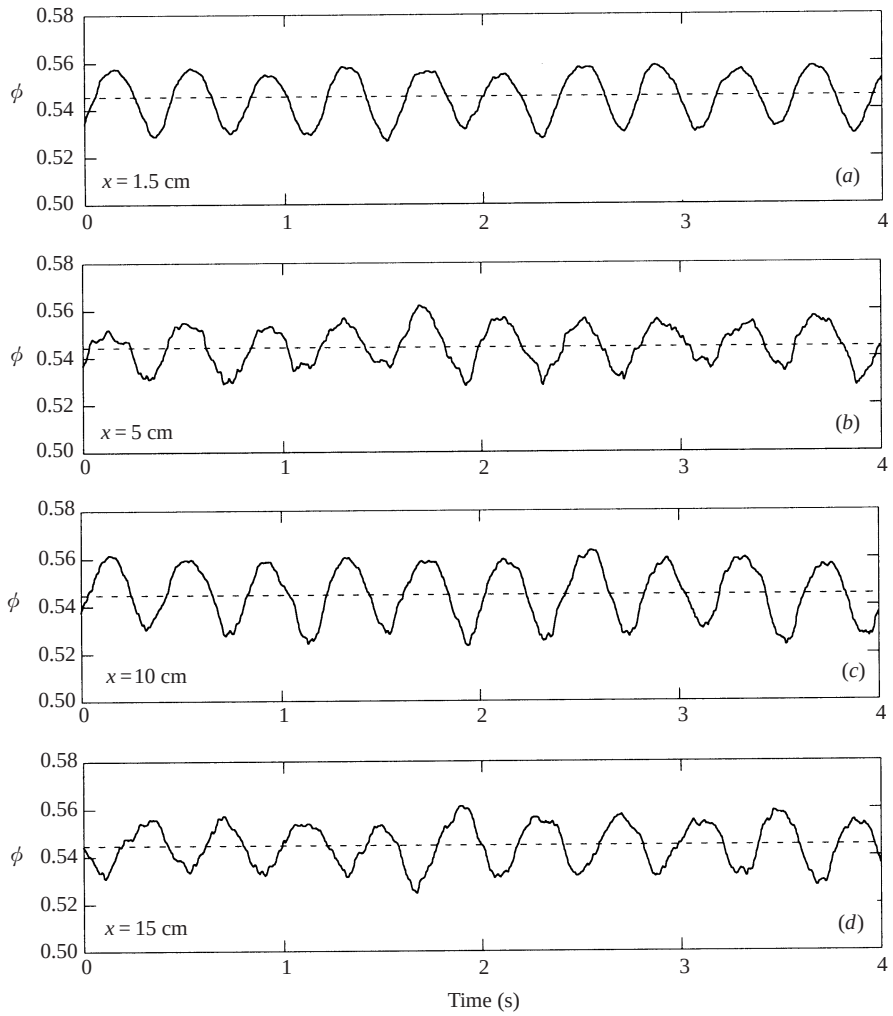

FIGURE 6. Spatial evolution of a neutral mode. This neutral mode was obtained when using combination 1 of particles, fluid and tube, with $\phi_0 = 0.545 \pm 0.005$ and $f_0 = 2.6$ Hz. The wave shape was measured at different positions x along the bed and obtained by averaging over 30 time sequences.

slightly lower than ϕ_c, but it has also to be greater than concentrations corresponding to turbulent regime. Consequently, the ϕ_0-range for which waves can be measured is limited. Once the mean particle concentration is fixed by adjusting the flow rate, the forcing frequency f_0 is chosen. It has to be below the neutral frequency f_n (at the given ϕ_0) but also above $\frac{1}{2}f_n$, to avoid secondary minima as mentioned in the preceding section. Again, this leads to a limited range of forcing frequency (typically between 1 Hz and 2 Hz). The viscosity value was only changed by a factor of 3, see table 3, because the wave amplitudes were very small and difficult to detect for larger values (see the discussion below).

For a given frequency, changing ϕ_0 does not modify significantly the shape of the saturated wave. Figure 11 shows the shape of three of the saturated waves obtained with combination 2, for different ϕ_0 but with the same f_0; the wave amplitude is slightly larger at lower concentrations and its velocity higher (see table 8 for

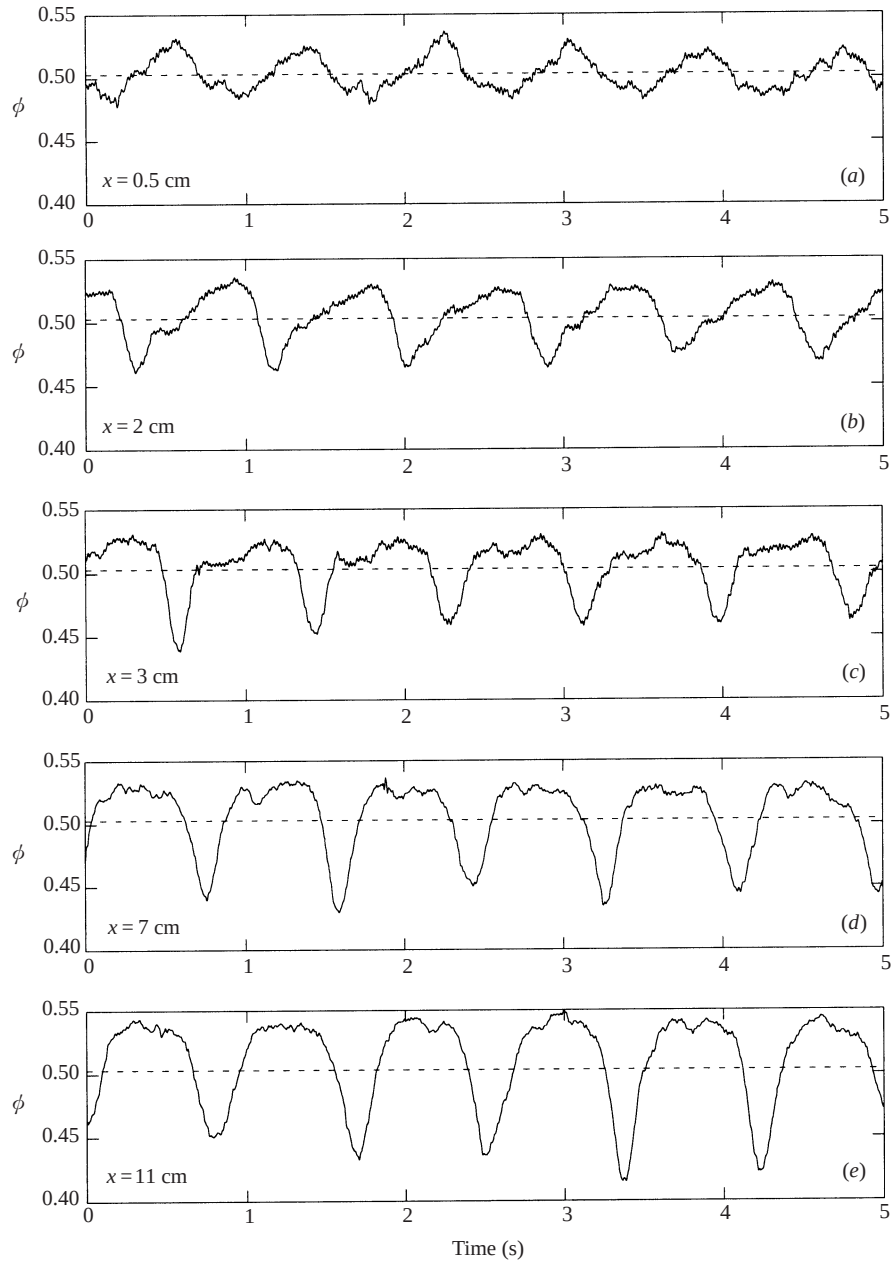

FIGURE 7. Spatial evolution of an unstable mode. This unstable mode was obtained when using combination 7 of particles, fluid and tube, with $\phi_0 = 0.503 \pm 0.002$ and $f_0 = 1.17$ Hz. The wave shape was measured at different positions x along the bed and obtained by averaging over 30 time sequences.

combination 3). Conversely, for a given mean particle concentration, changing the forcing frequency f_0 influences greatly the wave shape. As the frequency increases, the amplitude and wave velocity decrease, the wave becomes more and more symmetrical, and centred around the mean concentration. This can be seen in figure 12 which shows three of the saturated waves of combination 6, measured for different f_0 but with

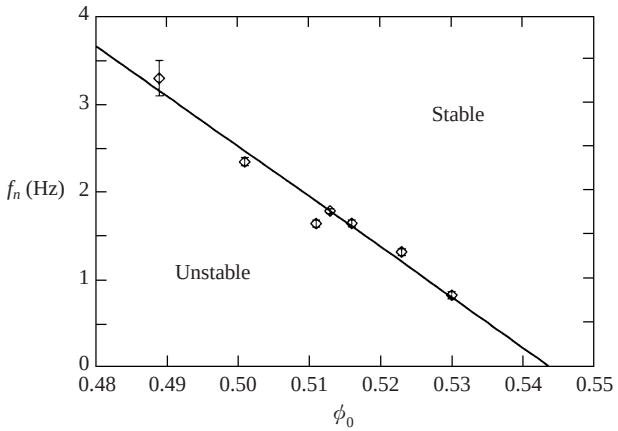

FIGURE 8. Stability diagram obtained for combination 7.

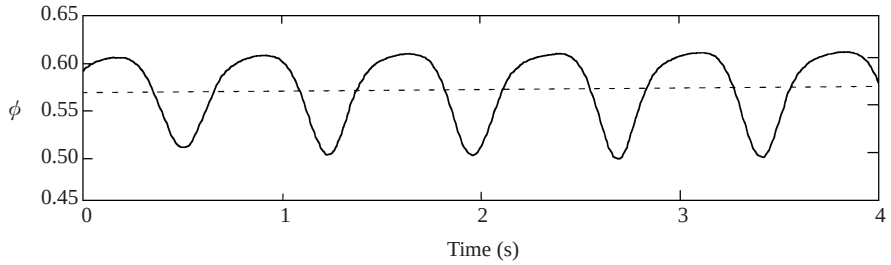

FIGURE 9. Saturated wave obtained for combination 7 with $\phi_0 = 0.57 \pm 0.005$ and $f_0 = 1.4$ Hz. This saturated wave was obtained by averaging over 100 time sequences.

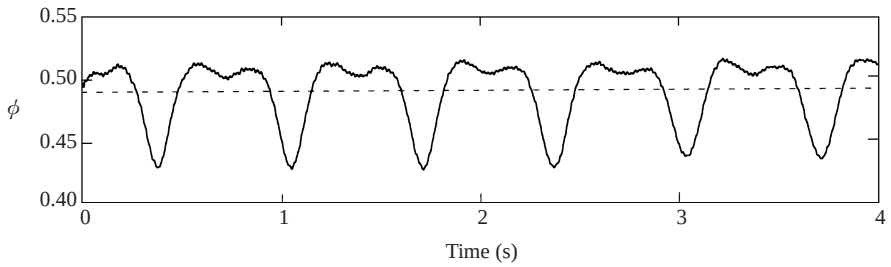

FIGURE 10. Wave showing a secondary minimum, obtained for combination 7 with $\phi_0 = 0.49 \pm 0.005$ and $f_0 = 1.5$ Hz. This saturated wave was obtained by averaging over 150 time sequences.

the same ϕ_0. It is not surprising because, as $f_0 \to f_n$, the shape of the wave becomes closer to that of a neutral mode, that is, by definition, a symmetrical sinusoidal wave with an amplitude equal to that of the forcing.

Increasing the fluid viscosity (by a factor 3 in the present case) has two main effects. First, the instability threshold ϕ_c is slightly modified (see table 7). Waves are thus measured in a more dilute bed with fluid *b* than with fluid *a*. Secondly, it reduces the wave amplitude (by a factor 2 in the present case). Figure 13 shows two waves obtained with fluids *a* and *b*, respectively. It should be noticed that the forcing frequency is different for the two waves but, since it is far from the cutoff frequency

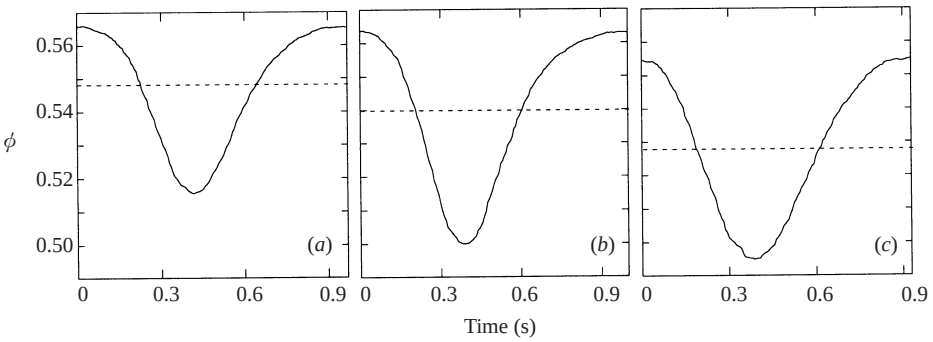

FIGURE 11. Influence of the mean particle concentration ϕ_0 on the shape of the saturated wave: (*a*) $\phi_0 = 0.548$; (*b*) $\phi_0 = 0.540$; (*c*) $\phi_0 = 0.528$. These waves were obtained with combination 2. Only one period of the wave is shown. The forcing frequency f_0 is ≈ 1.1 Hz for the three waves. The dashed line shows the mean particle concentration ϕ_0.

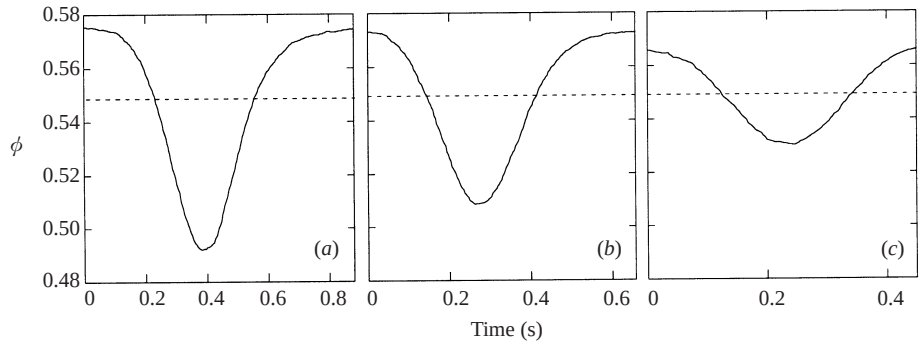

FIGURE 12. Influence of the forcing frequency f_0 on the shape of the saturated wave: (*a*) $f_0 = 1.1$ Hz; (*b*) $f_0 = 1.55$ Hz; (*c*) $f_0 = 2.2$ Hz. These waves were obtained with combination 6. Only one period of the wave is shown. The mean particle concentration ϕ_0 is 0.549 ± 0.003 for the three waves. The dashed line shows the mean particle concentration ϕ_0.

$f_n(\approx 2\,\text{Hz})$ in both cases, we can assume that the difference of amplitude between the wave of figure 13(*a*) and the wave of figure 13(*b*) is due to the difference in fluid viscosity only. It should be mentioned that when comparing figures 13(*a*) and 13(*b*), only the wave amplitude and c are modified (see table 8), the shape of the saturated wave remaining similar. It must also be noted that for fluid *b*, no state of stable homogeneous fluidization was observed. We also tried to use a more viscous fluid (a mixture of glycerin and water giving a viscosity $\mu_f = 5 \pm 0.2$ cP). A state of stable homogeneous fluidization was found in that case (for further details on the existence of stable fluidization with very viscous fluid or with light particles see Ham *et al.* 1990). Above the instability threshold ϕ_c, some voidage waves were observed, but they were of very small amplitude. It was, however, impossible to measure their shape precisely by averaging over a reasonable number of time sequences, because the signal to noise ratio was too small.

When changing the set of particles, the overall shape of the waves remains similar whereas amplitude of the waves and wave velocity c change, as can be seen in table 8. The remarks made above regarding the dependence of the saturated wave shape on ϕ_0, f_0, and μ_f are still relevant.

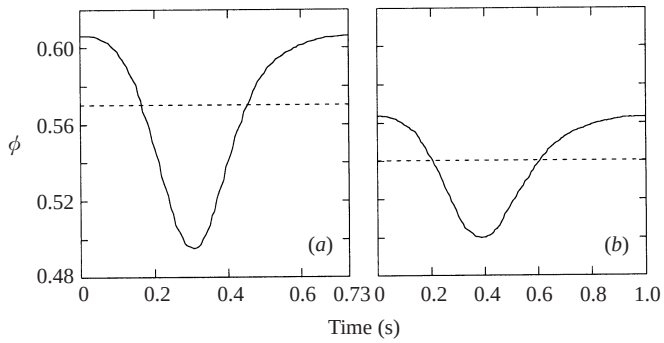

FIGURE 13. Influence of the fluid viscosity μ_f on the shape of the saturated wave: (*a*) wave of combination 1: $\phi_0 = 0.57$, $f_0 = 1.4\,\mathrm{Hz}$, $\mu_f = 0.9\,\mathrm{cP}$; (*b*) wave of combination 2: $\phi_0 = 0.54$, $f_0 = 1\,\mathrm{Hz}$, $\mu_f = 3\,\mathrm{cP}$. The dashed line shows the mean particle concentration ϕ_0.

4. Nonlinear analysis of the saturated unstable waves

We now present the two-phase equations we used for the analysis of the experimental data. The fluidized bed is described as a mixture of two continuous phases. For simplicity, both phases have a Newtonian rheology. The goal of this analysis is the determination of the solid phase viscosity μ_s and of the derivative of the solid pressure $\mathrm{d}p_s/\mathrm{d}\phi$ from the shape of the saturated wave.

4.1. *The saturated wave equation*

We chose to use the model of Anderson & Jackson (1967), more recently described in Anderson, Sundaresan & Jackson (1995), as the basic equations. The fluid phase has local velocity $u(x,t)$, density ρ_f, viscosity μ_f, and pressure p_f. The solid phase is also described as a fluid, with local velocity $v(x,t)$, density ρ_s, viscosity μ_s, and pressure p_s. The phases are coupled by a drag force and an added-mass force of the fluid phase acting on the solid phase. Since the fluid is a liquid rather than a gas, the added mass term cannot be neglected in the present case.

The full three-dimensional equations are described in Anderson *et al.* (1995). For the purpose of the present study, we reduce the dimensionality to one. In that case, the two-phase equations have the following form:

$$\frac{\partial \phi}{\partial t} + \frac{\partial}{\partial x}(\phi v) = 0, \tag{4.1}$$

$$-\frac{\partial \phi}{\partial t} + \frac{\partial}{\partial x}[(1-\phi)u] = 0, \tag{4.2}$$

$$\phi(\rho_s + \hat{C}\rho_f)\left(\frac{\partial v}{\partial t} + v\frac{\partial v}{\partial x}\right) - \phi\rho_f(1+\hat{C})\left(\frac{\partial u}{\partial t} + u\frac{\partial u}{\partial x}\right) + \frac{\partial p_s}{\partial x}$$
$$= \frac{4}{3}\frac{\partial}{\partial x}\left(\mu_s\frac{\partial v}{\partial x}\right) + \beta(u-v) - \phi(\rho_s - \rho_f)g, \tag{4.3}$$

where (4.1) and (4.2) are the mass conservation equations and (4.3) is the momentum equation for the solid phase. We do not write the momentum equation for the fluid phase as it is not needed in the following nonlinear analysis of the waves.

Adding and integrating the two continuity equations gives the mean flow rate q

which is the experimental control parameter:

$$q = \phi v + (1 - \phi)u. \tag{4.4}$$

The first two terms on the left-hand side of equation (4.3) are inertial terms coming from the solid and fluid phases, respectively. The third term is the unknown solid pressure gradient. The parameter $\hat{C} = C(\phi)/(1 - \phi)$ is the reduced added mass coefficient. The added mass coefficient $C(\phi)$ takes the value $\frac{1}{2}$ for an isolated particle. Of course, there is a concentration dependence but it is not fully understood.

The first term on the right-hand side of equation (4.3) is the viscous term, with, at this stage, an unknown solid viscosity μ_s. The second term on the right-hand side represents the drag force of the fluid acting on the solid phase. The coefficient $\beta(\phi)$ is the drag coefficient that can be deduced from the Richardson–Zaki law:

$$\beta(\phi) = \frac{(\rho_s - \rho_f)g}{v_t} \frac{\phi}{(1 - \phi)^{n-1}}, \tag{4.5}$$

where the two parameters v_t and n are determined from the expansion curve of the fluidized bed (see § 3.1). The last term on the right-hand side of equation (4.3) is the weight corrected for buoyancy.

Crude estimates of the different terms in equation (4.3) show that the weight corrected for buoyancy balances drag within a few per cent. Taking $\mathrm{d}p_s/\mathrm{d}\phi \sim$ 1–100 c.g.s., as suggested by Anderson & Jackson (1969) and Homsy, El-Kaissy & Didwania (1980), inertial and solid pressure terms can be estimated to be of comparable size. They represent less than 10% of the difference between drag and the weight corrected for buoyancy. Thus, the difference between drag and the weight corrected for buoyancy roughly equilibrates the solid viscous term.

If we now assume (as observed in the experiments) that a saturated wave travels in the fluidized bed at a constant velocity c, equations (4.1), (4.3) and (4.4) can be rewritten in a moving reference frame. The wave is stationary in this new reference frame with a space coordinate X defined by:

$$X = x - ct. \tag{4.6}$$

We also introduce the new velocities $u(X) = u(x, t) - c$ and $v(X) = v(x, t) - c$ and the volume fraction $\phi(X) = \phi(x, t)$. Using equations (4.1), (4.4) and (4.3), it is then possible to eliminate u and v successively and to write a single equation for the volume fraction ϕ. In the reference frame attached to the wave, the saturated wave equation has the form:

$$\tfrac{4}{3}c\phi_0 \frac{\mathrm{d}}{\mathrm{d}X}\left[\mu_s(\phi)\frac{\mathrm{d}\phi}{\mathrm{d}X}\frac{1}{\phi^2}\right] + F_1(\phi) + \left[F_2(\phi) - \frac{\mathrm{d}p_s}{\mathrm{d}\phi}\right]\frac{\mathrm{d}\phi}{\mathrm{d}X} = 0, \tag{4.7}$$

where

$$F_1(\phi) = \phi\rho_s \frac{g(\rho_s - \rho_f)}{\rho_s}\left[\frac{v_t(1 - \phi_0)^n - c(1 - \phi_0/\phi)}{v_t(1 - \phi)^n} - 1\right], \tag{4.8}$$

and

$$F_2(\phi) = \rho_f\phi(1 + \hat{C}(\phi))\frac{[v_t(1 - \phi_0)^n + c(\phi_0 - 1)]^2}{(1 - \phi)^3} + (\rho_s + \rho_f\hat{C}(\phi))\left(\frac{c\phi_0}{\phi}\right)^2. \tag{4.9}$$

The function $F_1(\phi)$ contains the difference between drag and the weight corrected for buoyancy. $F_2(\phi)$ groups inertial and added mass terms. The first term in F_2 is much smaller than the second, representing at best 15% of the total.

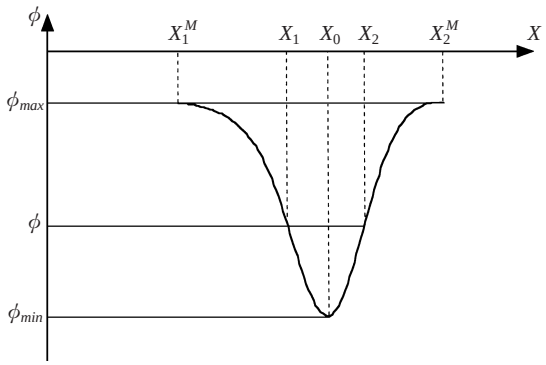

FIGURE 14. A saturated wave period plotted as a function of X. The quantities ϕ, ϕ_{max}, ϕ_{min}, X_0, X_1 and X_2 introduced in § 4.2 are shown.

4.2. *Determination of* μ_s *and* $\mathrm{d}p_s/\mathrm{d}\phi$

The two unknown functions of concentration, μ_s and $\mathrm{d}p_s/\mathrm{d}\phi$, can be determined from the shape of the wave $\phi(X)$ and its first derivative. The integration of equation (4.7) between two coordinates X_1 and X_2 such as $\phi(X_1) = \phi(X_2) = \phi$ (see figure 14) gives:

$$\frac{4\phi_0 c}{3\phi^2}\left[\left(\frac{\mathrm{d}\phi}{\mathrm{d}X}\right)_{X_2}\mu_s(\phi(X_2)) - \left(\frac{\mathrm{d}\phi}{\mathrm{d}X}\right)_{X_1}\mu_s(\phi(X_1))\right] = -\int_{X_1}^{X_2} F_1(\phi(X))\,\mathrm{d}X. \qquad (4.10)$$

This equation shows that the difference between the solid viscous stress at X_2 and X_1 balances the integral of the difference between drag and the weight corrected for buoyancy over the same interval.

The solid phase viscosity is thus given by:

$$\mu_s(\phi) = \frac{3}{4\phi_0 c}\frac{\phi^2}{(\mathrm{d}\phi/\mathrm{d}X)_{X_1} - (\mathrm{d}\phi/\mathrm{d}X)_{X_2}}\int_{X_1}^{X_2} F_1(\phi(X))\,\mathrm{d}X. \qquad (4.11)$$

Using this formula, $\mu_s(\phi)$ can be computed in the range $\phi_{min} < \phi < \phi_{max}$ for each measured saturated wave. Once $\mu_s(\phi)$ is known, we can differentiate equation (4.7) to find $[F_2(\phi) - \mathrm{d}p_s/\mathrm{d}\phi]$ within the same range of concentration. Thus, our fully non-linear analysis of the shape of the saturated waves provides a determination of $\mu_s(\phi)$ and $\mathrm{d}p_s/\mathrm{d}\phi$ (under assumptions concerning $C(\phi)$ in order to compute $F_2(\phi)$), which are the two unknown functions of concentration introduced in the two-phase modelling.

Equation (4.10) requires a good accuracy in the calculation of the first derivative of $\phi(X)$. Despite the precision in the measurement of the shape of the wave provided by the averaging method, experimental results are too noisy to compute directly the first derivative of $\phi(X)$. Experimental results were therefore fitted by an analytical periodic function, provided by a nonlinear least-squares fit algorithm implemented in the MatLab software. As a fitting function we have chosen a periodic quartic B-spline over 10 subintervals. As an example of many further observations, figure 15 shows the good agreement between the experimental wave and the fitted curve. All the results presented in the next sections were obtained using the fitted analytical function.

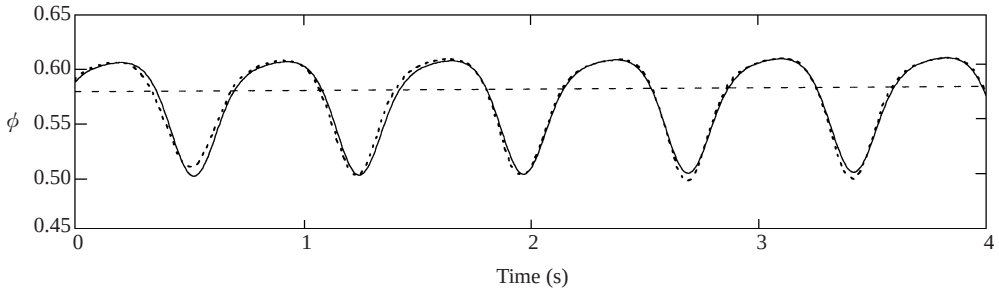

FIGURE 15. Example of a saturated wave fitted by a B-spline function. The saturated wave was obtained for combination 1 with $\phi_0 = 0.57 \pm 0.005$ and $f_0 = 1.4\,\text{Hz}$. The dashed line is the experimental result and the solid line is the fitting B-spline function.

5. Determination of the solid phase viscosity μ_s

In this section, we present the results concerning the solid viscosity $\mu_s(\phi)$. For each of the measured saturated waves, we used formula (4.11) to compute $\mu_s(\phi)$. We hereafter study the influence of experimental parameters on $\mu_s(\phi)$.

5.1. *Influence of ϕ_0 and f_0 on μ_s*

Figure 16(*a*,*b*) shows the function $\mu_s(\phi)$ for waves shown in figures 11 and 12. For waves of figure 11, only the mean particle concentration ϕ_0 was changed, the wave frequency being roughly constant. Conversely, ϕ_0 was fixed and the forcing frequency f_0 was varied for waves of figure 12.

The solid viscosity $\mu_s(\phi)$ is found to be an increasing function of the particle concentration ϕ. The solid viscosity increases strongly as ϕ approaches ϕ_{max}. It is therefore more convenient to plot $1/\mu_s$ as a function of ϕ. This is done in figure 16(*c*,*d*) which shows the same results as in figure 16(*a*,*b*). The solid viscosity seems to vary as ϕ^{-1}, which was not obvious in figure 16(*a*,*b*) showing μ_s against ϕ. Note also the plot of $1/\mu_s$ against ϕ has the useful side effect of making the larger error bars at high ϕ appear smaller, because the relative error was not so large.

The solid viscosity does not seem to vary significantly with the mean particle concentration ϕ_0, as can be seen on figure 16(*a*), at least for the limited range of ϕ_0 in which voidage waves were measurable. Differences for 'low' concentration between the wave at $\phi_0 = 0.528$ (circle in figure 16*a*,*c*) and the two others are displayed more clearly when we plot $1/\mu_s$ as a function of ϕ, see figure 16(*c*), but they are still within the large error bars. In the other cases studied, for example waves of combination 1 and 3 (see table 8), the differences have been also observed to be small and within error bars.

The solid viscosity does not seem to vary significantly with f_0, in the range of frequencies examined. For waves of figure 16(*b*,*d*), the two curves for $f = 1.1\,\text{Hz}$ and $f = 1.55\,\text{Hz}$ are different, but it is not significant because of the large error bars involved. However, as can be seen in figure 16(*d*), the slope difference is much larger for the quasi-neutral mode at $f = 2.2\,\text{Hz}$, but the data are still within the error bars of the two other curves. Concerning this last curve, we can wonder if we really measured a saturated wave as, when we approach the cutoff frequency f_n, the time (and thus the distance covered in the bed) taken by the wave to saturate should increase strongly. It is therefore possible that this saturated state was not reached in our bed of limited height. This could explain why results for this quasi-neutral mode are slightly different.

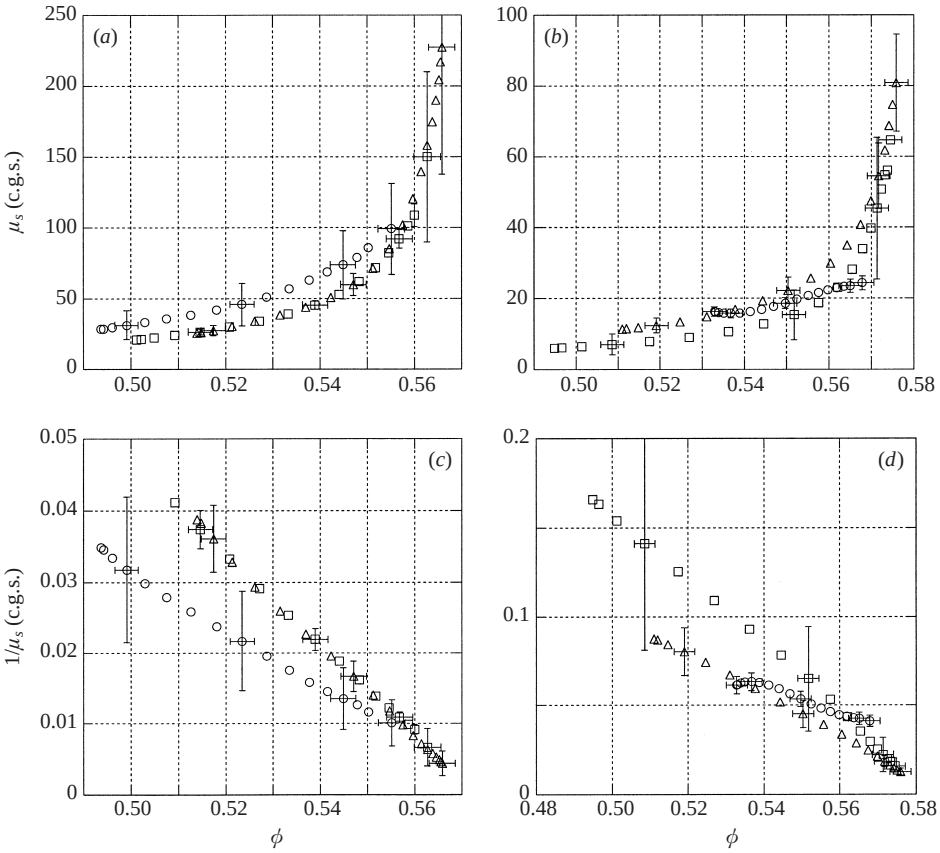

FIGURE 16. Influence of the mean particle concentration ϕ_0 and of the forcing frequency f_0 on μ_s. (*a*) μ_s plotted against ϕ for combination 2, at $f_0 = 1$ Hz; △, $\phi_0 = 0.548$; □, $\phi_0 = 0.540$; ○, $\phi_0 = 0.528$. (*b*) μ_s plotted against ϕ for combination 6, at $\phi_0 = 0.549$; □, $f_0 = 1.1$ Hz; △, $f_0 = 1.55$ Hz; ○, $f_0 = 2.2$ Hz. (*c*) $1/\mu_s$ as a function of ϕ, same curves as in (*a*). (*d*) $1/\mu_s$ as a function of ϕ, same curves as in (*b*).

The fact that the solid viscosity does not seem to vary with frequency supports the modelling of the stresses of the solid phase by a Newtonian viscous fluid without any elastic component of stress.

5.2. *Influence of fluid viscosity on* μ_s

We now consider the influence of the fluid viscosity μ_f on $\mu_s(\phi)$. The fluid viscosity μ_f has been increased by a factor 3 from combination 1 to combination 2. It must be stressed that the ϕ-range 'probed' in the present experiments, that is the typical interval $[\phi_{min}, \phi_{max}]$ for which μ_s can be computed owing to equation (4.11), is not the same for waves of combinations 1 and 2. As already mentioned, the instability threshold ϕ_c for fluid *b* is slightly smaller than that for fluid *a*. Therefore, the mean particle concentrations ϕ_0 for which saturated waves can be measured, are smaller for fluid *b* (see table 8). The interval $[\phi_{min}, \phi_{max}]$ being roughly centred around ϕ_0, this results in a shift along the ϕ-axis between curves showing $1/\mu_s(\phi)$ for viscous fluid *b* and for fluid *a*, see figure 17(*a*). It is then difficult to compare directly the solid viscosity obtained in each case and to draw conclusions from the apparent difference between the two families of curves.

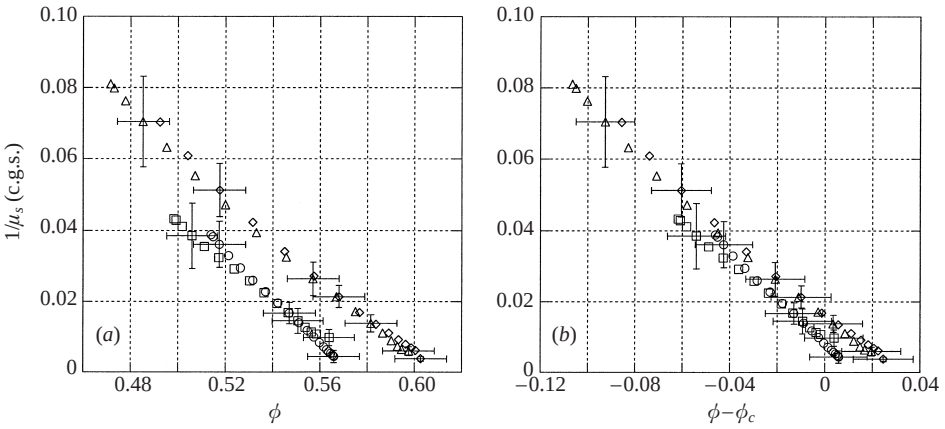

FIGURE 17. Influence of the fluid viscosity μ_f on μ_s. (*a*) $1/\mu_s$ plotted against ϕ; (*b*) $1/\mu_s$ plotted against $\phi - \phi_c$; ○, $\phi_0 = 0.548$; □, $\phi_0 = 0.538$: combination 2 with $\mu_f = 3\,\text{cP}$ and $\phi_c = 0.560$. ◇, $\phi_0 = 0.558$; △, $\phi_0 = 0.55$: combination 1 with $\mu_f = 0.9\,\text{cP}$ and $\phi_c = 0.578$.

If we now plot $1/\mu_s$ as a function of $\phi - \phi_c$ instead of ϕ, all curves collapse into a single curve, as can be seen in figure 17(*b*). It then becomes clear that the solid viscosity does not scale with the fluid viscosity. The differences between the two families of curves in figure 17(*a*) can be interpreted as a shift of our measurement zone resulting from the shift in ϕ_c caused by the change in fluid viscosity. The collapse obtained when plotting $1/\mu_s$ as a function of $\phi - \phi_c$ means that the bed rheological behaviour, as far as μ_s is concerned, is controlled at a given ϕ by the distance to the instability threshold.

5.3. *Influence of D/d_s on μ_s*

In this section, we compare the solid viscosity for waves of combinations 6 and 7. Only the bed to particle diameter ratio D/d_s differs from combination 6 to combination 7, see table 8. The resulting curves are presented in figure 18. Once again, the ϕ-ranges for which $\mu_s(\phi)$ is computed are not the same for waves of combinations 6, 7 and the resulting shift along the ϕ-axis is large, see figure 18(*a*). This shift is not only due to the change in threshold ϕ_c (see table 7), but also to the fact that waves were measured 'further' above the instability threshold for combination 7 (as mentioned in § 3.1). This latter point is not corrected if we plot $1/\mu_s$ as a function of $\phi - \phi_c$ and a significant shift between curves of combination 7 and curves of combination 6 remains. Therefore, we must plot $1/\mu_s$ as a function of $\phi - \phi_0$ for the shift to disappear, as can be seen in figure 18(*b*).

It must be emphasized that for all combinations, excepted combination 7, aspect ratio D/d_s was between 17 and 25 so that waves were measured near ϕ_c. The case of combination 7 is thus rather particular but important because it makes more obvious the relevance of cancelling shifts along the ϕ-axis before comparing the values of $\mu_s(\phi)$ for different combinations. However, it could also mean that for combination 7, the ratio D/d_s is too small and that our results are strongly influenced by wall effects.

5.4. *Scaling law for μ_s*

It remains for us to consider the influence of particle characteristics on $\mu_s(\phi)$. By comparing combinations 3 and 8, we can study the influence of the particle diameter d_s on $\mu_s(\phi)$. By comparing combinations 2 and 3, we can study the influence of particle

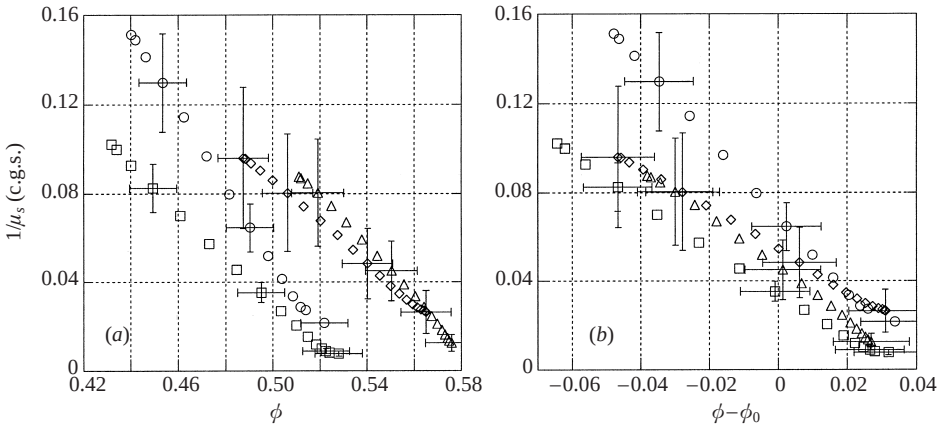

FIGURE 18. Influence of the bed to particle ratio D/d_s on μ_s. (*a*) $1/\mu_s$ plotted against ϕ; (*b*) $1/\mu_s$ plotted against $\phi-\phi_0$. ○, $\phi_0 = 0.488$; □, $\phi_0 = 0.496$: combination 7 with $D/d_s \approx 10$. △, $\phi_0 = 0.549$; ◇, $\phi_0 = 0.534$: combination 6 with $D/d_s \approx 25$.

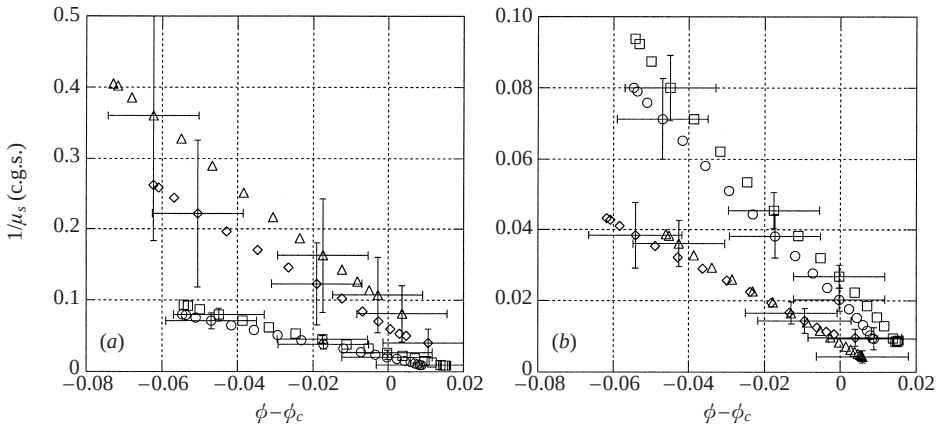

FIGURE 19. Influence of the characteristics of the beads on μ_s. (*a*) $1/\mu_s$ plotted against $\phi-\phi_c$; □, $\phi_0 = 0.535$; ○, $\phi_0 = 0.545$: combination 3 with $d_s v_t = 1.7$ c.g.s. and $\phi_c = 0.555$. ◇, $\phi_0 = 0.530$; △, $\phi_0 = 0.521$: combination 8 with $d_s v_t = 0.9$ c.g.s. and $\phi_c = 0.544$. (*b*) $1/\mu_s$ plotted against $\phi-\phi_c$; □, $\phi_0 = 0.535$; ○, $\phi_0 = 0.545$: combination 3 with $\rho_s v_t = 36$ c.g.s. and $\phi_c = 0.555$. △, $\phi_0 = 0.548$; ◇, $\phi_0 = 0.538$: combination 2 with $\rho_s v_t = 83$ c.g.s. and $\phi_c = 0.560$.

density ρ_s on $\mu_s(\phi)$. The difficulty is that the terminal velocity v_t also changes when ρ_s and/or d_s are changed. For example, for combinations 2 and 3, v_t is decreased by a factor of 50% while ρ_s is decreased by a factor of 60%.

We can see in figure 19(*a*) that, for a similar ϕ-range (which is ensured by plotting $1/\mu_s$ as a function of $\phi-\phi_c$), $\mu_s(\phi)$ is increased when $d_s v_t$ is increased for a given particle density ρ_s. Similarly, in figure 19(*b*), we can see that $\mu_s(\phi)$ is increased when $\rho_s v_t$ is increased for a given particle size d_s.

Several combinations of the parameters of the bed can be constructed with the dimensions of viscosity. We have plotted μ_s made dimensionless by $\rho_s d_s v_t$ in figure 20(*a*) and by $\rho_f d_s v_t$ in figure 20(*b*). A good collapse into a single curve is obtained in both cases. Unfortunately, large experimental error-bars do not allow us to discriminate between these two scalings even though the scatter of the data seems smaller in

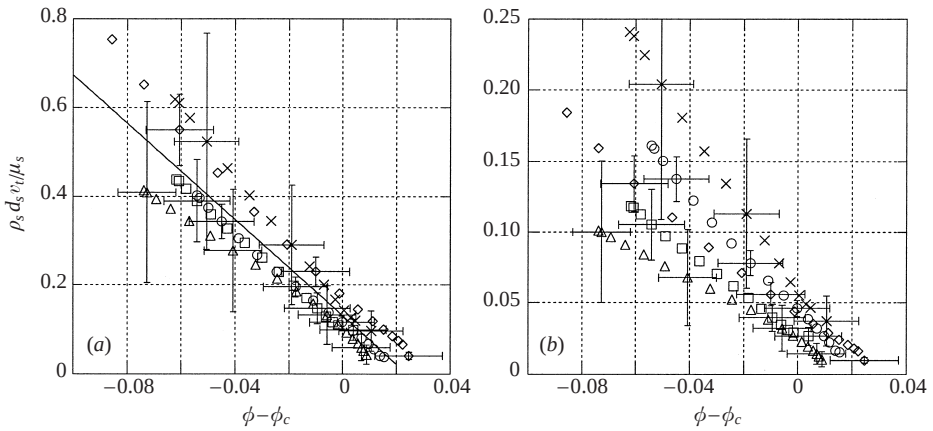

FIGURE 20. Scaling laws for μ_s: (*a*) $\rho_s d_s v_t/\mu_s$ as a function of $\phi - \phi_c$ for a representative sample of curves, the solid line shows the best fitting linear function for all these data; (*b*) $\rho_f d_s v_t/\mu_s$ as a function of $\phi - \phi_c$. ◇, $\phi_0 = 0.558$, combination 1 with $\phi_c = 0.578$; □, $\phi_0 = 0.538$, combination 2 with $\phi_c = 0.560$; ○, $\phi_0 = 0.545$, combination 3 with $\phi_c = 0.555$; △, $\phi_0 = 0.549$, combination 6 with $\phi_c = 0.555$; ×, $\phi_0 = 0.530$, combination 8 with $\phi_c = 0.544$.

figure 20(*a*). In the same way, scaling μ_s by $(\rho_s - \rho_f)d_s v_t$ or $(\rho_s \rho_f)^{1/2} d_s v_t$ would also provide similar good collapses.

To try to distinguish between these different possible scaling, we can refer to rheological measurements of stress in fluidized bed (for a good review, see Schügerl 1971). Effective viscosities measured in suspensions fluidized by air or a liquid are about the same size. This leads us to feel inclined towards a scaling involving the solid density *via* ρ_s or the difference $\rho_s - \rho_f$ rather than the fluid density ρ_f alone.

As a conclusion of this section, it should be stressed that the interpretation of our data was complicated by shifts along the ϕ-axis between curves corresponding to different combinations owing to fluid viscosity effects (see § 5.2) or confinement effects (see § 5.3). We resolved to correct these effects first, and then to compare curves giving $1/\mu_s(\phi)$. The solid viscosity seems to vary as ϕ^{-1} and to diverge for values of concentration between $\phi_c + 0.02$ and $\phi_c + 0.04$, see figure 20(*a*), which corresponds roughly to a random loose packing of the bed. In the limited range of f_0, ϕ_0 and μ_f studied, we propose finally the best linear fit displayed in figure 20(*a*) as a scaling law for μ_s:

$$\mu_s(\phi) \approx 0.18 \frac{\rho_s d_s v_t}{\phi_{rlp} - \phi}. \tag{5.1}$$

The best linear fit gives the prefactor 0.18 and the value $\phi_{rlp} \approx \phi_c + 0.025$ for which μ_s diverges which can be considered as a random loose-packing concentration. Unfortunately, ϕ_{rlp} is not a well-defined physical quantity.

This scaling works for the results obtained with all combinations except combination 7. To take into account this last set of results, we should have introduced a dependence of the results with ϕ_0. It is therefore a pity that the ϕ_0-range probed for other combinations was so small that it was not possible to detect an hypothetical discrepancy between curves giving μ_s when ϕ_0 was varied. It would have then validated another kind of more complex scaling, involving ϕ_0. However, as we have already mentioned, it is also possible that results obtained for set 7 are affected too strongly by wall friction and thus are not relevant.

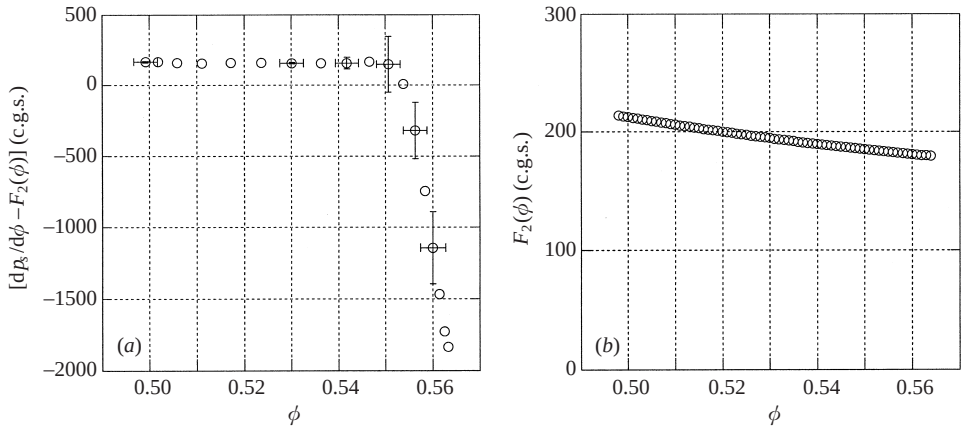

FIGURE 21. (*a*) $[dp_s/d\phi - F_2(\phi)]$ as a function of ϕ for the wave of combination 2 with $\phi_0 = 0.538$; (*b*) $F2(\phi)$, computed with $C = \frac{1}{2}$, for the wave of combination 2 with $\phi_0 = 0.538$.

6. Determination of the solid pressure derivative $dp_s/d\phi$

The present nonlinear analysis of the saturated waves also provides some insight concerning $dp_s/d\phi$. As explained in § 4.2, we can compute $[dp_s/d\phi - F_2(\phi)]$ for values of ϕ in the interval $[\phi_{min}, \phi_{max}]$. A typical curve is shown in figure 21(*a*). The quantity $[dp_s/d\phi - F_2(\phi)]$ is first constant for a large range of ϕ but, as ϕ approaches ϕ_{max}, the slope abruptly becomes negative and $[dp_s/d\phi - F_2(\phi)]$ decreases strongly as ϕ increases, when $0.55 < \phi < 0.564 = \phi_{max}$. This can also be seen owing to the following calculation. Multiplying equation (4.7) by $\mu_s(\phi) \times (d\phi/dX) \times 1/\phi^2$ and then integrating from X_1^M to X_2^M (see figure 14) leads to:

$$\int_{X_1^M}^{X_2^M} \mu_s(\phi) \left[F_2(\phi) - \frac{dp_s}{d\phi} \right] \left(\frac{d\phi}{dX} \frac{1}{\phi} \right)^2 dX = 0, \tag{6.1}$$

which proves that $[dp_s/d\phi - F_2(\phi)]$ must change its sign. The experimental curve of figure 21(*a*) indeed shows that the sign of this expression is first positive and then becomes negative. We can also see that for a perfectly symmetrical wave, we would have obtained $F_2(\phi) = dp_s/d\phi$, see equation (4.7), which means that the solid pressure gradient would compensate exactly the inertial terms in this hypothetical case. The slight asymmetry of the measured wave therefore means that $dp_s/d\phi$ is not exactly equal to $F_2(\phi)$ at all ϕ.

It is possible to compute $dp_s/d\phi$ by simply adding $F_2(\phi)$ to $[dp_s/d\phi - F_2(\phi)]$. Calculations have been made taking $C(\phi) = \frac{1}{2}$. A typical curve for $F_2(\phi)$ is shown in figure 21(*b*).

6.1. *Influence of* ϕ_0 *on* $dp_s/d\phi$

Figure 22(*a*) shows $dp_s/d\phi$ for three waves of combinations 2, shown in figure 11. Only the mean particle concentration ϕ_0 differs from one wave to another. For each curve, we encounter the same behaviour as in figure 21(*a*): $dp_s/d\phi$ is roughly constant for a large range of ϕ before decreasing when concentrations near ϕ_{max} are reached. The value of $dp_s/d\phi$ in the constant part is approximately the same for each curve. The quantity $dp_s/d\phi$ begins to decrease for $\phi = 0.53$ when $\phi_0 = 0.528$ (circles on figure 22*a*), whereas it begins to decrease for $\phi = 0.55$ when $\phi_0 = 0.548$ (diamonds on 22*a*). This small shift along the ϕ-axis is meaningful because it is not within

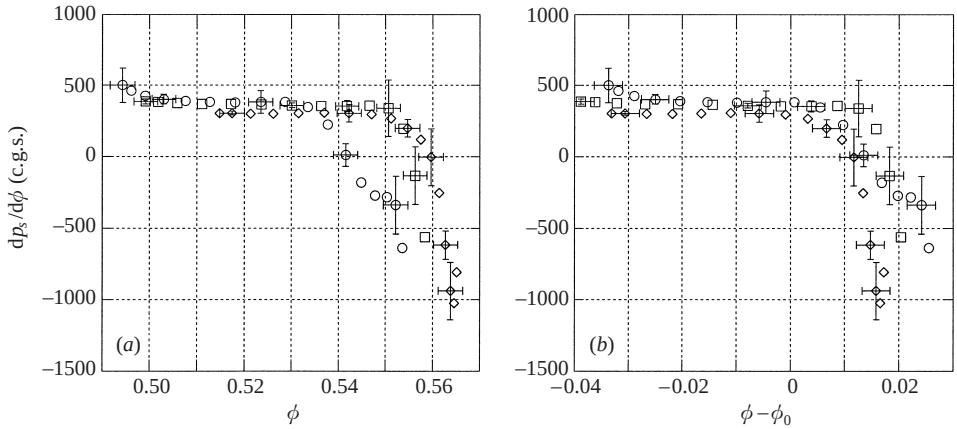

FIGURE 22. Influence of the mean particle concentration ϕ_0 on $dp_s/d\phi$: (*a*) $dp_s/d\phi$ for combination 2 as a function of ϕ; (*b*) $dp_s/d\phi$ for combination 2 as a function of $\phi - \phi_0$. ◇, $\phi_0 = 0.548$; □, $\phi_0 = 0.538$; ○, $\phi_0 = 0.528$.

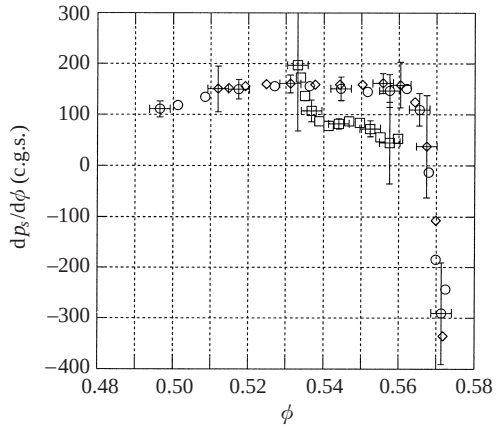

FIGURE 23. Influence of the forcing frequency f_0 on $dp_s/d\phi$: $dp_s/d\phi$ for combination 6 as a function of ϕ. ○, $f_0 = 1.1$ Hz; ◇, $f_0 = 1.55$ Hz; □, $f_0 = 2.2$ Hz.

errors bars. This shift disappears if we now plot $dp_s/d\phi$ as a function of $\phi - \phi_0$, see figure 22(*b*). Owing to the relatively small ϕ_0-range probed by our experiments, we were not able to confirm this result by measuring saturated waves and thus $dp_s/d\phi$ for mean particle concentrations lower than 0.528 which could have made the shift along the ϕ-axis greater. It is important to repeat that no noticeable differences were found in $\mu_s(\phi)$ for different ϕ_0, see figure 16(*a*).

6.2. *Influence of* f_0 *on* $dp_s/d\phi$

Figure 23 shows $dp_s/d\phi$ for waves shown in figure 12. Only the forcing frequency f_0 differs from one wave to another. For the waves measured at $f_0 = 1.1$ Hz and $f_0 = 1.55$ Hz (circles and diamonds, respectively, in figure 23), the two curves are similar, with a decrease of $dp_s/d\phi$ when ϕ approaches ϕ_{max}. For the wave measured at $f_0 = 2.2$ Hz (square in figure 23), the data differ slightly from those of the two other curves. We have already suggested in § 5.1 that it could be due to the fact that the corresponding wave was not fully saturated when it was measured.

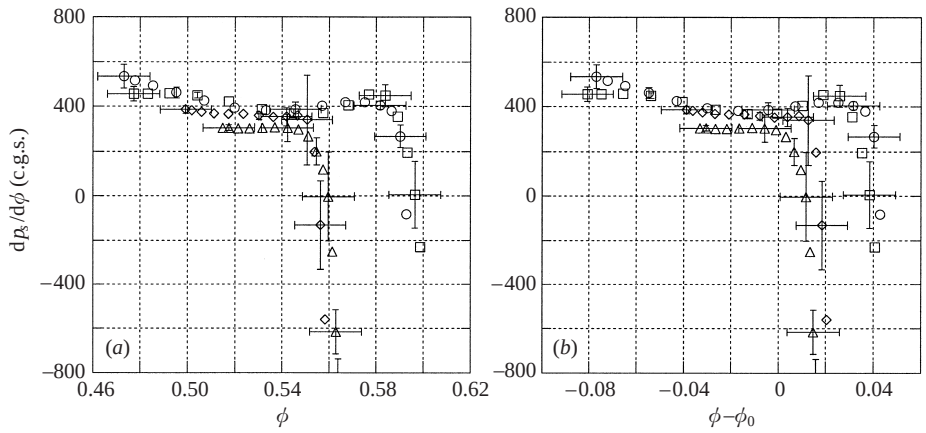

FIGURE 24. Influence of the fluid viscosity μ_f on $dp_s/d\phi$: (*a*) $dp_s/d\phi$ plotted against ϕ; (*b*) $dp_s/d\phi$ plotted against $\phi - \phi_0$. △, $\phi_0 = 0.548$; ◇, $\phi_0 = 0.538$: combination 2 with $\mu_f = 3$ cP. □, $\phi_0 = 0.558$; ○, $\phi_0 = 0.55$: combination 1 with $\mu_f = 0.9$ cP.

6.3. *Influence of* μ_f *on* $dp_s/d\phi$

Figure 24(*a*) shows $dp_s/d\phi$ for waves of combinations 1 and 2. Only the fluid viscosity μ_f differs from combination 1 to combination 2. Each curve presents a decrease of $dp_s/d\phi$ when ϕ approaches ϕ_{max}. The value of $dp_s/d\phi$ in the constant part is approximately the same for each curve.

To compare the results obtained with fluid *a* with those obtained with fluid *b*, we have the same problem as that raised while dealing with the influence of μ_f on $\mu_s(\phi)$: the intervals $[\phi_{min}, \phi_{max}]$ differ with the fluid viscosity. Waves were obtained in a relatively more dilute bed with viscous fluid *b* and their amplitudes were half of those obtained with fluid *a*. Nonetheless, we have seen in § 5.2 that plotting $\mu_s(\phi)$ as a function of $\phi - \phi_c$ instead of ϕ (see figure 17), was sufficient to obtain a collapse of curves into a single one, showing that the apparent differences were mainly due to the influence of the fluid viscosity μ_f on the instability threshold ϕ_c (ϕ_c for combination 2 is lower than ϕ_c for combination 1).

However, in the present case, because we have seen in § 6.1 that there was a small influence of ϕ_0 on $dp_s/d\phi$, we decided to plot $dp_s/d\phi$ as a function of $\phi - \phi_0$ rather than $\phi - \phi_c$, see figure 24(*b*). Notice that plotting $dp_s/d\phi$ as a function of $\phi - \phi_c$ would have given the same kind of plot, regarding the relative position of each family of curves because waves were measured roughly at the same distance from the instability threshold ϕ_c in combinations 1 and 2. In fact, using $\phi - \phi_0$ instead of $\phi - \phi_c$ brings changes only regarding the relative position of curves of the same combination. In figure 24(*b*) showing $dp_s/d\phi$ as a function of $\phi - \phi_0$, only a small offset along the ϕ-axis nonetheless remains, which means that the change in fluid viscosity also brings a change in the amplitude of the waves.

6.4. *Influence of* D/d_s *on* $dp_s/d\phi$

We now plot $dp_s/d\phi$ for combinations 6 and 7. Only the bed to particle diameter ratio D/d_s differs in combinations 6 and 7. Figure 25(*a*) shows $dp_s/d\phi$ as a function of ϕ. The origin of the shift along the ϕ-axis between curves computed from waves of combination 6 and curves computed from waves of combination 7 has already been explained in § 5.3. The value of the constant part of function $dp_s/d\phi$ is roughly

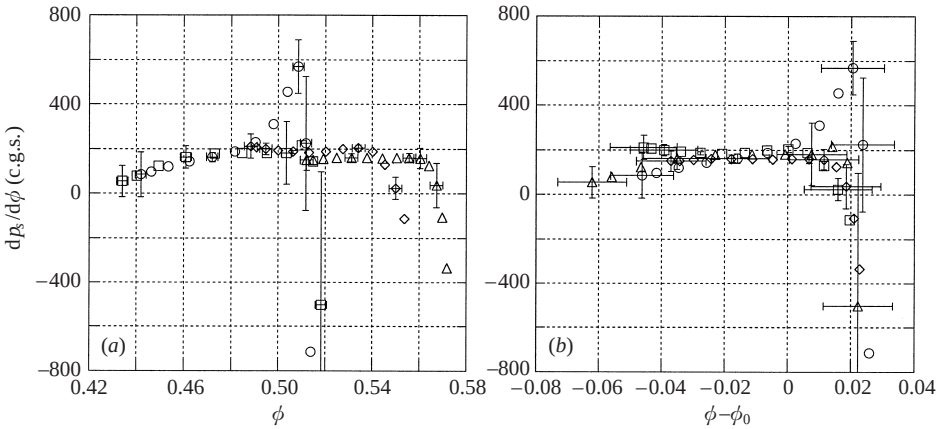

FIGURE 25. Influence of the bed to particle ratio D/d_s on $\mathrm{d}p_s/\mathrm{d}\phi$: (*a*) $\mathrm{d}p_s/\mathrm{d}\phi$ plotted against ϕ; (*b*) $\mathrm{d}p_s/\mathrm{d}\phi$ plotted against $\phi - \phi_0$. ○, $\phi_0 = 0.488$; □, $\phi_0 = 0.496$: combination 7 with $D/d_s \approx 10$. △, $\phi_0 = 0.549$; ◇, $\phi_0 = 0.534$: combination 6 with $D/d_s \approx 25$.

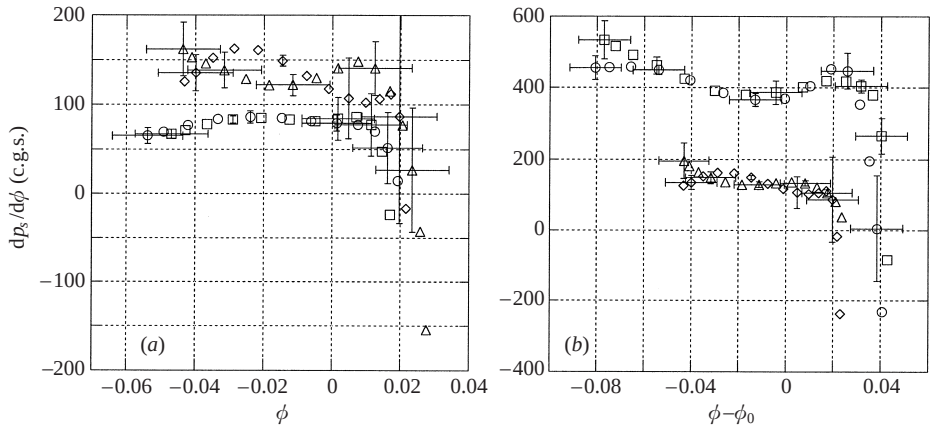

FIGURE 26. Influence of the characteristics of the beads on $\mathrm{d}p_s/\mathrm{d}\phi$: (*a*) $\mathrm{d}p_s/\mathrm{d}\phi$ as a function of $\phi - \phi_0$; △, $\phi_0 = 0.535$; ◇, $\phi_0 = 0.545$: combination 3 with $d_s v_t = 1.7$ c.g.s.; □, $\phi_0 = 0.530$; ○, $\phi_0 = 0.521$: combination 8 with $d_s v_t = 0.9$ c.g.s. (*b*) $\mathrm{d}p_s/\mathrm{d}\phi$ as a function of $\phi - \phi_0$; △, $\phi_0 = 0.535$; ◇, $\phi_0 = 0.545$: combination 3 with $\rho_s v_t = 36$ c.g.s.; □, $\phi_0 = 0.558$; ○, $\phi_0 = 0.550$: combination 1 with $\rho_s v_t = 88$ c.g.s.

the same for all curves. We obtain a good collapse into a single curve when plotting $\mathrm{d}p_s/\mathrm{d}\phi$ as a function of $\phi - \phi_0$, see figure 25(*b*).

6.5. *Scaling laws for* $\mathrm{d}p_s/\mathrm{d}\phi$

Now it remains to study the influence of particle characteristics on $\mathrm{d}p_s/\mathrm{d}\phi$. Figure 26(*a*) shows curves obtained with waves of combinations 3 and 8. The quantity $\mathrm{d}p_s/\mathrm{d}\phi$ is plotted as a function of $\phi - \phi_0$. It is clear that the value of the constant part of $\mathrm{d}p_s/\mathrm{d}\phi$ is greater when $d_s v_t$ is larger. In the same way, in figure 26(*b*), which shows curves obtained with waves of combination 1 and 3, we see that this value is greater when $\rho_s v_t$ is larger.

We thus plotted $\mathrm{d}p_s/\mathrm{d}\phi$ made dimensionless by $\rho_s v_t^2$ on figure 27(*a*) and by $\rho_f v_t^2$ on figure 27(*b*). These two graphs show that $\mathrm{d}p_s/\mathrm{d}\phi$ seems to scale with $\rho_s v_t^2$ or $\rho_f v_t^2$. Because of the scatter of the data, it is not possible to discriminate between these two

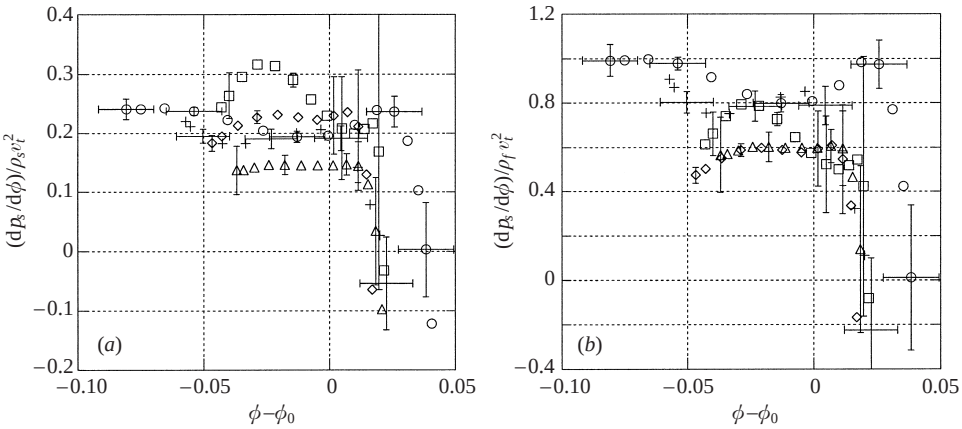

FIGURE 27. Scaling laws for $\mathrm{d}p_s/\mathrm{d}\phi$: (*a*) $(\mathrm{d}p_s/\mathrm{d}\phi)/\rho_s v_t^2$ as a function of $\phi-\phi_0$ for a representative sample of curves; (*b*) $(\mathrm{d}p_s/\mathrm{d}\phi)/\rho_f v_t^2$ as a function of $\phi-\phi_0$. ○, $\phi_0 = 0.558$, combination 1; □, $\phi_0 = 0.545$, combination 3; ×, $\phi_0 = 0.527$, combination 4; △, $\phi_0 = 0.549$, combination 6; ◇, $\phi_0 = 0.530$, combination 8.

scalings. In the same way, scaling μ_s by $(\rho_s-\rho_f)v_t^2$ would also provide a similar good collapse. In the limited range of f_0, ϕ_0 and μ_f studied, we can therefore propose the following scaling laws for $\mathrm{d}p_s/\mathrm{d}\phi$, for most of the ϕ:

$$\mathrm{d}p_s/\mathrm{d}\phi \approx 0.2\rho_s v_t^2, \quad \text{or} \quad \mathrm{d}p_s/\mathrm{d}\phi \approx 0.7\rho_f v_t^2. \tag{6.2}$$

7. Discussion

By forming long-time averages synchronized with periodic forcing applied at the base of the fluidized bed, we have been able to observe the growth up the bed of one-dimensional voidage waves to their saturated finite amplitude. These saturated waves have a well-defined shape, with flat peaks of high particle concentrations and narrow troughs of low concentrations. Their variation with frequency and average particle concentration has been reported in § 3.4. These observations are all available to benchmark future new theories and computer simulations.

We have chosen to interpret the observations of the saturated voidage waves in terms of the simplest two-phase model of fluidized beds. We have thus measured the viscosity and pressure of the solid phase and found how they vary with particle concentration. It must be pointed out that these measurements were made over a limited range of parameters and only for saturated finite-amplitude one-dimensional voidage waves. It remains to be seen if they are applicable to a wider class, for instance three-dimensional flows.

Results for the viscosity of the solid phase, $\mu_s(\phi)$, were reported in § 5. The viscosity was found not to depend on the frequency of the periodic forcing, which means that the stresses should be characterized by a constant Newtonian viscosity rather than an elasticity or a more complex rheology. The solid phase viscosity was further found to depend little on the viscosity of the suspending fluid μ_f, the liquid flow rate q or equivalently the average particle concentration ϕ_0, and the diameter of the tube D (except for combination 7 where the tube was narrow and for which wall-friction may have an effect). We found that the variation of the solid phase viscosity on the density ρ_s, diameter d_s and terminal velocity v_t of the particles and on the local

particle concentration could be approximated by the expression:

$$\mu_s(\phi) \approx 0.18 \frac{\rho_s d_s v_t}{\phi_{rlp} - \phi}. \tag{7.1}$$

This scaling law applies to the limited range of concentration in our experiments, $\phi > 0.5$, and indeed we would expect the solid phase viscosity μ_s to vanish as the concentration of the particles tends to zero. The evidence for the use of the particle density ρ_s in this expression instead of the density of the fluid ρ_f is not conclusive. We must recall here that our experiments are for liquid-fluidized beds with particles and liquid of similar density. In gas-fluidized beds, there would be a considerable difference between expression (7.1) and using the gas density ρ_f in place of the particle density ρ_s, with the latter option yielding more sensible values. We should also note here that the particle Reynolds number varies in our experiments over the range 20–200. We have not detected any simple variation with the Reynolds number, other than that used in the expression for the terminal velocity of an isolated particle v_t, but we certainly would expect a different behaviour at low particle Reynolds numbers.

The rapid increase in the solid phase viscosity as the concentration approaches the packing value ϕ_{rlp} explains the characteristic shape of the saturated voidage waves. When the particle concentration is equal to its mean value ϕ_0, there is an exact balance between the drag on the particles and their weight. At higher concentrations, the drag wins and at lower concentration the weight wins, with an approximately linear variation of the imbalance with concentration over the small range of concentrations in our waves. It is the viscous stresses which principally equilibrate these slight imbalances between the weight and the drag. The same size of imbalance is equilibrated over a longer lengthscale at the high viscosity of the higher concentrations compared with the shorter lengthscale at the low viscosity of the lower concentrations; hence, the characteristic shape of the saturated voidage waves occurs with wide flat peaks of high concentrations and narrow troughs of low concentrations.

From our expression for the solid phase viscosity in a fluidized bed, we can also make a simple order-of-magnitude estimate of the wavelength of the saturated voidage waves. We equate the imbalance between the weight and the drag $(\rho_s - \rho_f)g\Delta\phi$ with the viscous term in the equation of motion $\mu_s v_t (2\pi/\lambda)^2$, where $\Delta\phi$ is the amplitude of the concentration variations and λ is the wavelength. Substituting our expression for the solid phase viscosity and the high-Reynolds-number estimate for the terminal velocity $v_t^2 \approx 0.8(\rho_s - \rho_f)g d_s/\rho_f$, we obtain:

$$\lambda \approx \frac{2.5\, d_s}{\Delta\phi} \sqrt{\frac{\rho_s}{\rho_f}}. \tag{7.2}$$

The wavelength is expected to be a large multiple of particle diameter and to be slightly longer for heavier particles, as qualitatively observed in table 8. It should not depend upon frequency and be shorter for larger-amplitude waves (not clearly observed in table 8 owing to the short ranges of forcing frequency and amplitude). It is possible that this prediction of our simple order-of-magnitude estimate will be significantly modified by a more careful solution of the governing equation.

The solid phase pressure along with the inertial terms in the governing equation are small compared with the imbalances between the drag and the weight. Hence, the asymmetry in the form of the saturated voidage wave, for which they alone are responsible, is small. It was therefore more difficult to obtain accurate measurements of the solid phase pressure. Thus, while it appears that $\mathrm{d}p_s/\mathrm{d}\phi$ is constant over most

of the range of concentrations, the precise form at the highest concentrations remains unclear for our experiments. There is of course the possibility near to the maximum concentration that solid–solid contacts are forming a continuous network which would produce stresses not described properly by a solid phase pressure depending only on the particle concentration. While the smallness of the stabilizing pressure and destabilizing inertial terms is inconvenient experimentally, their smallness leads to a useful simplification in a theoretical study, in which the shape of the wave is first determined ignoring these small terms and then afterwards the saturated amplitude is found from the integral balance (6.1) between the stabilizing and destabilizing effects.

Experimentally, we found in § 6 that the solid phase pressure did not depend on the frequency of the forcing. This means that a solid phase pressure varying with the particle concentration is a well-defined material property of a fluidized bed; at least, in the restricted range of our experiments. We also found that the solid phase pressure, like the solid phase viscosity, varied little with the viscosity of the liquid μ_f, the average particle concentration ϕ_0, and the diameter of the bed (except for the very narrow bed in combination 7). The variation with the density ρ_s, diameter d_s, and terminal velocity v_t of the particles seems to be described by the expression:

$$\mathrm{d}p_s/\mathrm{d}\phi \approx 0.7\rho_f v_t^2, \quad \text{or} \quad \mathrm{d}p_s/\mathrm{d}\phi \approx 0.2\rho_s v_t^2, \tag{7.3}$$

over a range of most of the concentrations, with large negative values at the highest concentrations. Figure 27 does, however, display a large variation around the value 0.7, with values 0.5 and 0.9 suiting certain results better. It is unclear whether there is a systematic trend, say with the particle Reynolds number, between the different experiments which we have not detected, or whether the differences are just a reflection of the large experimental uncertainty in determining this small quantity. With the large variation between our results for the solid phase pressure, the choice between the alternative expressions $\mathrm{d}p_s/\mathrm{d}\phi \approx 0.7\rho_f v_t^2$ and $\mathrm{d}p_s/\mathrm{d}\phi \approx 0.2\rho_s v_t^2$ remains open. However, a strong dependence of the stabilizing term with ρ_s was observed by Ham *et al.* (1990).

Our experimental finding that $\mathrm{d}p_s/\mathrm{d}\phi$ is a positive constant for most concentrations before decreasing sharply to negative values at the highest concentrations is very different from all the expressions which have been proposed before in theoretical studies, see table 1. The previously proposed expressions have the pressure increasing monotonically, and mostly increasing sharply at the highest concentrations. As a consequence, our slightly asymmetric one-dimensional wave has a higher slope of concentrations when increasing in time compared with when decreasing, whereas previous theoretical studies had the opposite asymmetry (see for example Anderson *et al.* 1995). The traditional justification of these increasing expressions has been a consideration of the stability of the fluidized bed. Fluidized beds are more stable at higher concentrations†. In the competition between the stabilizing effects of pressure and destabilizing effects of inertia, it was therefore natural to expect the pressure to increase strongly at high concentrations. This argument for the pressure overlooked the behaviour of the destabilizing inertial terms. In order to explain the greater stability of concentrated beds, when the pressure term $\mathrm{d}p_s/\mathrm{d}\phi$ is constant as we have found, we must observe that the inertial terms can decrease as the concentration increases.

† Of course, at very high concentrations, the particles are in continuous contact, and under these conditions the particle pressure cannot be related to the local value of the concentration but instead is determined globally by the need to avoid further compaction of the bed.

This decrease accompanies the decrease in the kinematic wave speed $v_t\phi_0 n(1-\phi_0)^{n-1}$ at higher concentrations.

As we have discussed above, the pressure term $\mathrm{d}p_s/\mathrm{d}\phi$ might be either $0.7\rho_f v_t^2$ or $0.2\rho_s v_t^2$. If the correct expression is the former, then the stabilizing pressure term would be proportional to the density of the fluid ρ_f while the destabilizing inertial term is proportional to the density of the particle ρ_s (plus an added mass term proportional to ρ_f) but with a smaller coefficient. In such circumstances we would speculate that there is a minimum density of the particles, around $1.5\rho_f$ for $n = 3$, for the destabilization to beat the stabilization at any concentration, i.e. fluidized beds of light particles would be stable.

In conclusion, we can say that while the simplest two-phase model of a fluidized bed might be misconceived from a theoretical point of view because simple expressions for the closures should not exist, it would appear that this simplest model is quite satisfactory for describing the one-dimensional voidage waves in the limited range of parameters that we have studied. It remains to be tested experimentally in more general flows, where for example an important role might be played by the large fluctuations in the bed which were averaged out by the sampling technique for the saturated wave.

We would like to thank R. Jackson for discussions during the course of this work. This work is part of the thesis of P. D. sponsored by the French Ministère de l'Éducation Nationale, de la Recherche et de la Technologie. It would not have been possible without the technical assistance of F. Ratouchniak, J.-C. Morellini and P. Cervetti.

REFERENCES

Anderson, T. B. & Jackson, R. 1967 Fluid mechanical description of fluidized beds. Equations of motion. *Ind. Engng Chem. Fundam.* **6**, 527–539.

Anderson, T. B. & Jackson, R. 1968 Fluid mechanical description of fluidized beds. Stability of the state of uniform fluidization. *Ind. Engng Chem. Fundam.* **7**, 12–21.

Anderson, T. B. & Jackson, R. 1969 Fluid mechanical description of fluidized beds. Comparison of theory and experiments. *Ind. Engng Chem. Fundam.* **8**, 137–144.

Anderson, K., Sundaresan, S. & Jackson, R. 1995 Instabilities and the formation of bubbles in fluidized beds. *J. Fluid Mech.* **303**, 327–366.

Batchelor, G. K. 1991 The formation of bubbles in fluidized beds. In *Proc. Honoring John W. Miles on his 70th Birthday*. Scripps Institution of Oceanography, Ref. Series 91–24.

Davidson, J. F. & Harrison, D. 1971 *Fluidization*. Academic.

Davis R. H. & Birdsell K. H. 1988 Hindered settling of semidilute monodisperse and polydisperse suspensions. *AIChE J.* **34**, 123–129.

Didwania, A. K. & Homsy, G. M. 1981 Flow regime and flow transitions in liquid-fluidized beds. *Intl J. Multiphase Flow* **7**, 563–580.

El-Kaissy, M. M. & Homsy, G. M. 1976 Instability waves and the origin of bubbles in fluidized beds. Part 1: experiments. *Intl J. Multiphase Flow* **2**, 379–395.

Fanucci, J. B., Ness, N. & Yen, R.-H. 1981 Structure of shock waves in gas-particulate fluidized beds. *Phys. Fluids* **24**, 1944–1954.

Glasser, B. J., Kevredikis, I. G. & Sundaresan, S. 1996 One- and two-dimensional travelling wave solutions in gas-fluidized beds. *J. Fluid Mech.* **306**, 183–221.

Glasser, B. J., Kevredikis, I. G. & Sundaresan, S. 1997 Fully developed travelling wave solutions and bubble formation in fluidized beds. *J. Fluid Mech.* **334**, 157–188.

Ham, J. M., Thomas, S., Guazzelli, É., Homsy, G. M., & Anselmet M.-C. 1990 An experimental study of the stability of liquid-fluidized beds. *Intl J. Multiphase Flow* **16**, 171–185.

Harris, S. E. & Crighton, D. G. 1994 Solitons, solitary waves, and voidage disturbances in gas-fluidized beds. *J. Fluid Mech.* **266**, 243–276.

Homsy, G. M. El-Kaissy, M. M. & Didwania, A. 1980 Instability waves and the origin of bubbles in fluidized beds. Part 2: comparison with theory. *Intl J. Multiphase Flow* **6**, 305–318.

Jackson, R. 2001 *Dynamics of Fluidized Particles.* Cambridge University Press.

Needham, D. J. & Merkin, J. H. 1983 The propagation of voidage disturbances in a uniform fluidized bed. *J. Fluid Mech.* **131**, 427–454.

Murray, J. D. 1965 On the mathematics of fluidization. Part 1. Fundamental equations and wave propagation. *J. Fluid Mech.* **21**, 465–493.

Nicolas, M., Chomaz, J.-M. & Guazzelli, É. 1994 Absolute and convective instabilities of fluidized beds. *Phys. Fluids* **6**, 3936–3944.

Nicolas, M., Chomaz, J.-M., Vallet, D. & Guazzelli, É. 1996 Experimental investigations on the nature of the first wavy instability in liquid–fluidized beds. *Phys. Fluids* **8**, 1987–1989.

Richardson, J. F. & Zaki, W. N. 1954 Sedimentation and fluidization. Part 1. *Trans. Inst. Chem. Engrs* **32**, 35–53.

Schügerl, K. 1971 Rheological behavior of fluidized systems. In *Fluidization* (ed. J. F. Davidson & D. Harrison), chap. 6. Academic.